IRE1 drives a homeostatic response to reduced protein influx into the endoplasmic reticulum

Francesca Zappa[1]*, Advait Subramanian[1]*, Benjamin Yang[2], Julia E. Conrad[1], Tsan-Wen Lu[1], Jing Wang[2], Nicolas A. DeBeaubien[1], Rose Yan[2], Renato Minopoli[3], Tristan Croll[3], Stefka Tyanova[2], Mauro Costa-Mattioli[1], Peter Walter[1†$], and Diego Acosta-Alvear[1†]

[1]Institute of Science, Altos Labs, Inc., Redwood City, CA, USA.
[2]Institute of Technology, Altos Labs, Inc., Redwood City, CA, USA.
[3]Institute of Medicine, Altos Labs, Inc., Redwood City, CA, USA.

*These authors contributed equally.

[†]To whom correspondence should be addressed:
dacostaalvear@walterlab.science, pwalter@walterlab.science.

[$]Present address: Department of Biochemistry and Biophysics, University of California at San Francisco, San Francisco, CA, USA.

Abstract

IRE1, alongside ATF6 and PERK, orchestrates the Unfolded Protein Response, a network of signaling pathways that maintains endoplasmic reticulum (ER) homeostasis. Two modes of IRE1 activation are known: i) in response to an accumulation of unfolded proteins in the ER lumen and ii) in response to compositional changes to the ER membrane that alter its physical properties. Here we identify a third, independent mode of IRE1 activation: ER co-translational translocation deficits activate IRE1 through a mechanism that relies on the release of IRE1 molecules from unoccupied translocons. We define this mechanism as TRES for “TRanslocon Engagement Surveillance”. TRES leads to spontaneous activation of IRE1 and bypasses its unfolded protein- and ER membrane composition-sensing functions. Inhibiting translation initiation similarly activates IRE1 by TRES, as it leads to a decline in ER protein import, thus linking the Integrated Stress Response to IRE1 signaling. TRES drives IRE1 activation without activating ATF6 or PERK, resulting in a distinct gene expression program that feeds back by boosting the co-translational translocation machinery to rebalance the ER protein load. Our findings thus demonstrate that monitoring and adjusting the rates of protein translocation are critical for maintaining ER homeostasis.

Introduction

Surveillance of protein targeting and import across organelle membranes is a fundamental process that ascertains that the protein folding load and the available protein folding machinery are properly balanced. In the endoplasmic reticulum (ER), protein targeting is facilitated by the signal recognition particle (SRP), which delivers translating ribosomes synthesizing signal sequence-bearing peptides to the translocon, initiating the co-translational translocation of nascent polypeptide chains into the ER lumen (*1–3*). The translocon is a multiprotein complex composed of SEC61α, β, and γ subunits and accessory factors (*4*). Dedicated ER quality control mechanisms counterbalance deviations from homeostasis to maintain proper ER physiology and adjust the organelle's functions according to need. A key ER quality control mechanism is the Unfolded Protein Response (UPR). The UPR is a signaling network that detects protein folding defects ("unfolded protein stress") as well as changes in ER membrane composition and fluidity ("lipid bilayer stress") to activate transcriptional programs that rebalance ER function (*5–7*). In animals, the UPR is governed by three ER membrane-resident sensors: the kinase PERK, the transcription factor ATF6, and the kinase/RNase IRE1. Of the three sensors, only IRE1 interacts with the SRP, the ribosome, and the translocon (*8*, *9*), yet the functional implications of these associations remain largely unclear (*8–15*).

Current models posit that IRE1 activation results from the direct binding of unfolded protein ligands to its ER lumenal domain (*16–19*), the reversible dissociation of the lumenal ER chaperone BiP/GRP78 from IRE1 (*20*), and the sensing of lipid bilayer stress by IRE1's transmembrane domain (*21–23*). In response to these perturbations, IRE1 molecules self-associate and *trans*-autophosphorylate, both a prerequisite for awakening its endoribonuclease activity. Active IRE1 initiates the non-conventional splicing of the *X-box binding protein 1* (*XBP1*) mRNA to generate the central UPR transcription factor XBP1s ("s" for spliced) (*24*) that upregulates the transcription of genes involved in protein folding, protein export, ER-associated degradation (ERAD), and lipid biosynthesis (*25–29*) in order to rebalance the ER's functional capacity. In

addition, activated IRE1 degrades ER-localized mRNAs through RIDD (regulated IRE1-dependent decay) (*30*) and RIDDLE (RIDD Lacking Endomotif) (*31*), thereby reducing the flux of proteins entering the ER. Through these actions, IRE1 mitigates ER stress (*32*–*34*). If this cannot be achieved and ER stress remains unmitigated, sustained IRE1 activity induces cell death (*35*–*37*). Given its fundamental role in making life/death decisions, it comes as no surprise that maladaptive IRE1 signaling is linked to the pathophysiology of multiple neurodegenerative, metabolic, and malignant diseases (*7*).

Along with RIDD and RIDDLE, the flux of proteins entering the ER lumen can also be adjusted by controlling protein synthesis. A prominent mechanism governing protein synthesis rates is the Integrated Stress Response (ISR). The ISR is a homeostatic signaling network that detects a myriad of stresses, including unfolded protein stress, and temporarily curtails protein synthesis by attenuating translation initiation (*38*). Translational control via the ISR can be imposed on a rapid time scale and thus provides the cell with enough time to adapt through changes in gene expression. The ISR is thus intimately intertwined with the UPR, as both stress responses share a common sensor, PERK. Besides PERK, three additional ISR stress-sensing kinases, GCN2, HRI and PKR, converge on phosphorylating the alpha subunit of eukaryotic initiation factor 2 (eIF2α). Phosphorylation of eIF2α leads to the translational suppression of the vast majority of mRNAs and consequently limits the protein load inside the ER (*38*, *39*).

Here, we describe TRES (for TRanslocon Engagement Surveillance) as a third and heretofore unrecognized mode of IRE1 activation that operates independent of IRE1's unfolded protein and lipid bilayer stress sensing modalities. TRES couples IRE1 activation to decreased ER protein influx. IRE1 activation by TRES results from co-translational translocation deficits elicited by insufficient ER protein targeting, translocon dysfunction, and fluctuating translation initiation rates, as occur upon induction of the ISR. These deficits dissociate IRE1 from the translocon, allowing for its activation. The transcriptional output resulting from TRES-activated IRE1 signaling is distinct from that of the classically defined UPR. The discovery of TRES thus expands the concept of ER

100 stress to include conditions resulting in ER *under*loading. These findings establish that
101 disrupted protein translocation into the ER is a distress signal sensed by IRE1.
102
103 **Results**
104
105 *Dissociation from the translocon derepresses IRE1 during TRES.*
106
107 To elucidate the functional interplay between IRE1α (IRE1 hereafter) and the ER co-
108 translational translocation machinery, we generated four mNeonGreen-tagged and
109 doxycycline (Dox)-inducible expression constructs (Fig. 1A):
110 i) IRE^{WT} (wild-type IRE1);
111 ii) $IRE1^{TAD}$ (for "translocon association deficient"). IRE1 with a ten amino acid
112 deletion, ΔE434-D443, that reduces its association with the translocon (*10*) (Fig.
113 S1A);
114 iii) $IRE1^{DAB}$ (for "deaf and blind"). IRE1 with a core lumenal domain deletion, ΔI19-
115 D408, which blocks its ability to bind to unfolded proteins and BiP ("blind"),
116 combined with a point mutation, W457A, that renders it unable to sense lipid
117 bilayer stress ("deaf") (*22*, *23*) (Fig. S1B); and
118 iv) $IRE1^{BTAD}$ (for "blind and translocon association deficient"). IRE1 with a large
119 deletion that removes its entire lumenal portion, including its translocon-binding
120 motif, ΔI19-D443, which prevents unfolded protein, BiP, and translocon binding
121 but retains lipid bilayer stress sensing (Fig. S1C).
122 The constructs were integrated into *IRE1*$^{-/-}$ U-2 OS (osteosarcoma) cells at a defined
123 genomic locus using the Flp-In system (*40*), thereby allowing comparable and regulated
124 transgene expression. Dox treatment (5 ng/mL) induced robust expression of the
125 transgenes, which we estimated to be between ~8- and ~16-fold over endogenous
126 IRE1 protein levels observed in parental U-2 OS cells (Fig. S1D-E) (*41*).
127
128 We monitored the dynamics of IRE1 activation in *IRE1*$^{-/-}$ cells expressing $IRE1^{WT}$
129 or $IRE1^{TAD}$ by challenging them with the *N*-linked glycosylation inhibitor tunicamycin
130 (Tm), an ER stress-inducing agent that promotes the buildup of unfolded proteins in the

131 ER lumen. Expression of IRE1^{WT} led to a basal *XBP1* mRNA splicing (26±9%) (Fig. 1B;
132 lane 2, Fig. S1F). This signal, observed in the absence of ER stress, is a result of the
133 overexpression level of the transgene. As expected from previous observations, *XBP1*
134 mRNA splicing was boosted after Tm treatment (82±8% at 4 hours) (Fig. 1B; lane 5,
135 Fig. S1F), before attenuating back to baseline (28±14% at 24 hours) (Fig. 1B; lane 7,
136 Fig. S1F) (*42*). Unexpectedly, expression of IRE1^{TAD} in the absence of ER stress led to
137 high *XBP1* mRNA splicing (77±4%) (Fig. 1B, lane 9, Fig. S1F). By contrast to the *XBP1*
138 mRNA splicing fold-changes (~4-fold) observed for IRE1^{WT} (Fig. 1B, compare lanes 2
139 and 5, Fig. S1F), ER stress induction in cells expressing IRE1^{TAD} did not induce
140 substantive *XBP1* mRNA splicing (~1.1-fold over wild-type) (Fig. 1B; compare lanes 9
141 and 12, Fig. S1F). Moreover, IRE1^{TAD} activity remained elevated and, surprisingly, did
142 not attenuate as observed for IRE1^{WT} (Fig. 1B; compare lanes 9 and 14, Fig. S1F). Both
143 IRE1^{WT} and IRE1^{TAD} abundance gradually decreased to similar degrees over the time
144 course of the experiment. Thus, a decrease in IRE1 protein levels does not explain the
145 differences in activity observed between the wild type and TAD mutant.
146
147 To assess the contributions of IRE1's unfolded protein and ER membrane stress
148 sensing, we next expressed IRE1^{BTAD} and IRE1^{DAB} and measured *XBP1* mRNA splicing.
149 The expression of IRE1^{BTAD}, which cannot bind to the translocon, was necessary and
150 sufficient to induce *XBP1* mRNA splicing both in the absence and after induction of ER
151 stress. However, splicing was less prominent than shown above for IRE1^{TAD} (28±2%)
152 (Fig. 1C, lanes 4-6, Fig. S1G), consistent with the notion that the lumenal domain
153 potentiates IRE1 multimerization, which results in signal amplification (*18*, *19*). By
154 contrast, the expression of IRE1^{DAB}, which can bind to the translocon, failed to induce
155 *XBP1* mRNA splicing both in the absence and after induction of ER stress (Fig. 1C;
156 lanes 1 – 3, Fig. S1G).
157
158 Together, the data presented so far suggest that IRE1 is derepressed upon dissociation
159 from the translocon (IRE1^{TAD} and IRE1^{BTAD}) and that the activity resulting from this
160 brake-release is independent of IRE1's lumenal unfolded protein sensing domain.
161

162 *IRE1 senses co-translational translocation defects during TRES.*
163
164 Previous work indicated that depleting SEC61 subunits or clogging translocons with
165 artificial reporter constructs activate IRE1 (*12*, *15*). Accordingly, translocon inhibitors
166 induce IRE1 activation in cells (*43–46*). To address whether a reduction of co-
167 translational translocation into the ER results in IRE1 activation by way of its
168 dissociation from the translocon, we disrupted ER co-translational translocation and
169 measured *XBP1* mRNA splicing resulting from IRE1 activation.
170
171 First, we pharmacologically inhibited the translocon with the small-molecule
172 inhibitor SEC61-IN-1 (compound A317 in (*47*)) in cells expressing $IRE1^{WT}$. These
173 experiments showed a dose-dependent increase in *XBP1* mRNA splicing (~2-fold to
174 ~3.5-fold over baseline) (Fig. 1D; lanes 3-6, Fig. S2A) with an accompanying reduction
175 in the association between IRE1 and SEC61α (Fig. 1E; compare lanes 2, 4, and 5). By
176 contrast, Tm treatment induced *XBP1* mRNA splicing without affecting the interaction
177 between IRE1 and SEC61α, as previously described (*9*, *48*) (Fig. 1E; lanes 2-3).
178 Strikingly, SEC61-IN-1 treatment also induced *XBP1* mRNA splicing in *IRE1*$^{-/-}$ cells
179 expressing $IRE1^{DAB}$ (25±3%) (Fig. 1D, lanes 11-12, Fig. S2A), similar to that observed
180 upon expression of $IRE1^{BTAD}$ (28±2%) (compare Fig. 1C, lanes 5 and 6, with Fig. 1D
181 lanes 11 and 12). Taken together, these data indicate that neither unfolded-protein
182 binding, nor BiP-dissociation, nor lipid bilayer stress sensing is required for IRE1 activity
183 upon treatment with SEC61-IN-1.
184
185 To confirm these conclusions, we treated cells with a different translocon
186 inhibitor, cyclotriazadisulfonamide (CADA), for which the molecular mechanism of action
187 has been defined structurally (*49*). Molecular docking onto SEC61α shows that CADA
188 occupies a pocket nested between the plug and the lateral gate of the channel (Fig.
189 S2B, top), as does SEC61-IN-1 (Fig. S2B, bottom). These analyses suggest that both
190 drugs occupy a similar pocket and stabilize the translocon in a conformation
191 incompatible with translocation. Indeed, CADA activated $IRE1^{WT}$, as shown by IRE1
192 autophosphorylation and the accumulation of XBP1s protein (Fig. 1F). These

193 observations were not restricted to our transgene experiments, as SEC61-IN-1 and
194 CADA induced XBP1s protein accumulation in parental U-2 OS cells expressing
195 endogenous IRE1 (Fig. S2C).
196
197 IRE1 activation involves the formation of higher order oligomers (*42*). Whereas
198 Tm treatment expectedly induced IRE1 foci (Fig. S3, arrows) in U-2 OS cells expressing
199 fluorescently tagged IRE1^{WT}, treatment with SEC61-IN-1 did not (Fig. S3). These
200 results suggest that large IRE1 assemblies do not form during TRES.
201
202 To orthogonally test the notion that inhibiting translocon activity induces IRE1, we
203 disrupted co-translational translocation by depleting the SRP subunit SRP54 in a
204 different cell line solely relying on endogenous levels of IRE1. We reasoned that
205 preventing ribosome targeting to the translocon in cells depleted of SRP would lead to
206 IRE1 activation. Indeed, SRP54 depletion with small interfering RNAs in H4
207 neuroglioma cells resulted in *XBP1* mRNA splicing (32±8%) (Fig. 1G, S2D),
208 corroborating previous results (*12*).
209
210 In a third orthogonal approach, we reduced ER translocation by interrupting
211 general translation initiation which impedes co-translational ribosome targeting to the
212 ER. To this end, we treated cells with the translation initiation inhibitors rocaglamide A
213 (RocA) and silvestrol, which clamp the eIF4A RNA helicase to 5' untranslated regions of
214 mRNAs and prevent efficient 43S ribosomal subunit scanning (*50*, *51*). Treatment with
215 RocA resulted in a reduced ribosome density on ER membranes, as confirmed by
216 electron microscopy (Fig. S4A). RocA treatment led to the dissociation of IRE1^{WT} from
217 the translocon and from ribosomal proteins (Fig. 2A), with a corresponding induction of
218 *XBP1* mRNA splicing (95±5%) (Fig. 2B, lane 5, Fig. S4B). RocA treatment similarly led
219 to the dissociation of IRE1^{DAB} from the translocon and ribosomal proteins (Fig. 2C) and
220 IRE1^{DAB} dependent *XBP1* mRNA splicing (45±5%, lane 5) (Fig. 2D, Fig. S4C).
221
222 Notably, RocA treatment minimally affected the already high *XBP1* mRNA
223 splicing activity of the translocon-binding-deficient IRE1^{TAD} mutant (Fig. 2E, Fig. S4D),

224 indicating that IRE1 dissociation from the translocon is sufficient for high IRE1 activity.
225 Accordingly, RocA treatment increased *XBP1* mRNA splicing by IRE1^{WT} to a degree
226 comparable to that elicited by Tm treatment (Fig. 2F, compare lanes 4-6), suggesting
227 that disrupting co-translational translocation activates IRE1^{WT} to the same extent as ER
228 stress. Indeed, RocA treatment induced IRE1 autophosphorylation (Fig. 2G) and XBP1s
229 protein accumulation (Fig. 2G, S4E), and RIDD (Fig. S4F). As we observed upon
230 SEC61-IN-1 treatment, RocA did not induce prominent IRE1 foci (Fig. S4H). High RocA
231 concentrations (1 μM) did not elevate XBP1s protein levels despite inducing *XBP1*
232 mRNA splicing due to a strong translation initiation block (Fig. S4G).
233
234 Similar to our experiments with SEC61-IN-1 and CADA, RocA treatment of U-2
235 OS cells expressing endogenous IRE1 elicited *XBP1* mRNA splicing, albeit modestly
236 when compared to IRE1^{WT} overexpression (Fig. 2F, compare lanes 1 and 3, and lanes
237 2 and 4). Treatment with Tm, however, induced high *XBP1* mRNA splicing in these cells
238 (Fig. 2F, compare lanes 1 to 2 and 5 to 6). We obtained similar results in H4
239 neuroglioma cells treated with silvestrol (Fig. S5A) and in *ex vivo* liver tissues of mice
240 treated with Zotatifin, a synthetic RocA analogue (Fig. S5B). Notably, and by contrast to
241 our observations with RocA and silvestrol, we detected no *XBP1* mRNA splicing after
242 treating U-2 OS cells with the elongation inhibitors cycloheximide (CHX) and emetine
243 (EME), which would stabilize ribosome-nascent chain complexes on translocons (*52*)
244 (Fig. S5C).
245
246 Notably, neither ATF6 nor PERK were activated by RocA, SEC61-IN-1 or CADA
247 (Fig. S5D), which as expected were both activated by the classical UPR inducer
248 dithiothreitol (DTT), a reducing agent that disrupts disulfide bonds, as indicated by ATF6
249 proteolytic processing and a change in PERK's electrophoretic mobility in SDS-PAGE
250 due to its autophosphorylation (Fig. S5D). We noted that the highest concentration of
251 SEC61-IN-1 reduced the protein levels of GFP-ATF6 and PERK (Fig. S5D, lane 12), but
252 not IRE1 (Fig. S2C, lane 5). It is possible that PERK and ATF6 molecules are no longer
253 inserted into the ER membrane under these conditions (*53*) or that they are selectively
254 degraded.

255

256 Taken together, our genetic and pharmacological experiments converge on a
257 model in which co-translational translocation defects preferentially activate IRE1 by
258 promoting its dissociation from SEC61. This activation modality is independent of
259 IRE1's canonical unfolded protein binding or lipid bilayer stress-sensing.

260

261 *The Integrated Stress Response selectively activates IRE1 by TRES.*

262

263 The findings above demonstrate that reduced translation initiation activates IRE1.
264 These observations raise the intriguing possibility that the ISR, which operates as a
265 master regulator of translation initiation and intimately connects to the UPR, could
266 activate IRE1. To address this notion, we activated the ISR directly using FKBP-PKR,
267 an engineered ISR kinase that can be activated by the drug-like small molecule FKBP
268 homodimerizer AP-20187 and leads to suppression of translation initiation (Fig. 3A,
269 S6A) (*54*, *55*). We chose PKR because it responds to viral infection and not to unfolded
270 protein buildup.

271

272 Indeed, FKBP-PKR activation with AP-20187 (referred to as ISR^{ON} hereafter)
273 activated IRE1 as assessed by multiple lines of evidence:
274 i) it disrupted the IRE1-translocon interaction (Fig. 3B, compare lanes 3 and 4);
275 ii) it induced IRE1 autophosphorylation (Fig. 3C – lanes 4 and 5);
276 iii) it induced *XBP1* mRNA splicing (Fig. 3C – lanes 4 and 5; S6B – lanes 5 and 6)
277 and upregulated XBP1s transcriptional target genes (Fig. S6C,D); and
278 iv) it activated RIDD, which was suppressed upon co-treatment with the IRE1
279 RNase inhibitor 4μ8C (Fig. 3D).

280

281 Because the ISR signals through eIF2 phosphorylation *(38)*, and to rule out
282 potential off-target effects of FKBP-PKR activation, we next overexpressed a
283 phosphomimetic mutant of the α-subunit of eIF2 bearing the S51D mutation, $eIF2\alpha^{S51D}$
284 (*54*). As occurred with our ISR^{ON} approach, overexpression of $eIF2\alpha^{S51D}$ (Fig. S6E) was
285 sufficient to induce IRE1 autophosphorylation and *XBP1* mRNA splicing (Fig. 3E),

286 upregulate XBP1s transcriptional targets (Fig. S6F, G), and activate RIDD (Fig. 3F),
287 corroborating that the ISR activates IRE1. Accordingly, treatment with ISRIB, a small
288 molecule that renders cells refractory to the effects of eIF2 phosphorylation (*56*),
289 reduced *XBP1* mRNA splicing (Fig. 3G) and XBP1s target expression (Fig. S6H, I), and
290 diminished RIDD (Fig. 3H) in ISR^{ON} cells.
291
292 As a third approach to induce the ISR, we induced mitochondrial stress to
293 activate the ISR kinase HRI with mitochondrial uncouplers (oligomycin and BTdCPU)
294 (*57–59*). We observed induction of *XBP1* mRNA splicing that was reduced by treatment
295 with ISRIB and 4μ8C (Fig. S6J, K). We note that ISR activation increased total *XBP1*
296 mRNA levels, in addition to activating *XBP1* mRNA splicing (Fig. 3C, 3E); both these
297 effects were dampened by ISRIB treatment (Fig. 3G). These results indicate that *XBP1*
298 mRNA abundance is autoregulated by the ISR (*25*), in addition to being regulated by
299 ATF6 upon UPR induction (*24*).
300
301 To rule out potential involvement of the other UPR sensors under ISR^{ON}
302 conditions, we measured the electrophoretic mobility of PERK and the induction of
303 ATF6's canonical target genes (*HSPA5/BiP* and *GRP94*). We observed no changes in
304 PERK's electrophoretic mobility in SDS-PAGE (Fig. 3I), suggesting that PERK does not
305 become phosphorylated. Similarly, the level of the *GRP94* mRNA remained unchanged
306 (Fig. S6L). By contrast, ISR^{ON} elevated *HSPA5* mRNA levels (Fig. 3J and S6C). This
307 result is easily reconciled because *HSPA5* transcription is regulated by both ATF6 and
308 XBP1s (*25*, *26*, *60*). To demonstrate directly the lack of ATF6's involvement in ISR^{ON},
309 we depleted ATF6 using CRISPRi or alternatively blocked its activation with Ceapin-A7,
310 a small molecule ATF6 inhibitor (Fig. 3J) (*61*). Neither manipulation affected the *HSPA5*
311 mRNA levels upon ISR^{ON} induction (Fig. 3J, right panel - compare bar 2 to bars 3 and
312 6). As expected for the effect solely resulting from ISR activation, ISRIB treatment
313 blunted *HSPA5* mRNA upregulation upon ISR^{ON} (Fig. S6I) confirming that ISR^{ON} does
314 not activate PERK or ATF6. Further supporting these conclusions, ISR^{ON} led to *XBP1*
315 mRNA splicing by $IRE1^{DAB}$ (Fig. 3K) and did not induce $IRE1^{WT}$ foci (Fig. S6M).
316

317 Together, these data indicate that the translation initiation block and
318 consequential co-translational protein translocation deficits imposed by the ISR lead to
319 a selective activation of IRE1 that do not require IRE1's canonical ER stress-sensing
320 modalities or the formation of large IRE1 oligomers.
321
322 *The IRE1-induced gene expression program differs between TRES and the UPR.*
323
324 The selective activation of IRE1 in response to co-translational translocation
325 deficits prompted us to ask whether IRE1 induces customized gene expression
326 programs to match specific physiological requirements. To address this concept, we
327 compared the IRE1-dependent gene expression programs of IRE1 knockout cells and
328 IRE1-expressing cells driven by unfolded protein buildup (elicited by Tm) with those
329 driven by ER translocation disruptions (elicited by RocA). We then corroborated the
330 results in a different cell line, ISR^{ON} H4 cells, in the absence or presence of 4μ8C.
331
332 Expectedly, a targeted analysis of *XBP1* mRNA reads in our RNA sequencing
333 datasets indicated the splicing of *XBP1* mRNA induced by both RocA and ISR^{ON}
334 treatments, thus orthogonally validating the RT-PCR results described above (Fig. S7A
335 – B).
336
337 Gene ontology (GO) term analyses of a subset of 1,495 mRNAs whose
338 expression levels changed significantly (Abs $\log_2$FC > 0.5) upon RocA treatment in
339 $IRE1^{WT}$ cells compared to knockout controls revealed an enrichment of genes involved
340 in translation and ER protein quality control. These processes included pathways that
341 regulate protein synthesis, targeting and translocation, folding, glycosylation, and export
342 (Fig. 4A, Fig. S8A). Similarly, comparing ISR^{ON} cells to 4μ8C-treated controls revealed
343 an enrichment of the same processes (Fig. 4B, Fig. S8B). These analyses reveal a
344 heretofore unrecognized IRE1-dependent gene expression program in response to co-
345 translational translocation deficits.
346

347 To ascertain that this IRE1-dependent gene expression program is distinct from
348 the IRE1 program induced by the UPR, we compared the expression changes of
349 mRNAs induced by RocA and dependent on IRE1 to those induced by Tm, focusing on
350 representative mRNAs in the prevalent GO categories. These analyses revealed unique
351 TRES- or UPR-specific gene expression programs in addition to a common TRES/UPR
352 gene expression program. The TRES-specific IRE1 program regulates genes involved
353 in post-transcriptional gene expression, including those encoding components of mRNA
354 splicing, maturation, export and decay, as well as ribosome assembly (Fig. 4C).
355 Notably, the TRES program also induced genes involved in regulating SRP-dependent
356 co-translational targeting and translocation, including those encoding translocon
357 subunits (*SEC61A1*, *SEC61B*, *SEC61G*), signal sequence receptor (*SSR1/2/3/4*), SRP
358 (*SRP68/72*), SRP receptor (*SRPRA*), signal peptidase (*SPCS1/2*) and the translocation-
359 associated membrane protein *TRAM1* (Fig. 4D). Conversely, the common TRES/UPR
360 gene expression program includes genes encoding chaperones, foldases, trafficking
361 machinery, and ERAD components (e.g., *HSPA5*, *HSP90B1*, *HYOU1*, *FICD*, *SYVN1*,
362 *SEC22B*, *SEC24D*, *EDEM1*, *DERL2*) (Fig. S8C). Notably, the activation of this common
363 program was exclusively dependent on IRE1 during TRES as several of these genes
364 are known XBP1s targets. During the UPR, however, IRE1 signaling was largely
365 dispensable for the upregulation of *RAB33B*, *HSP90B1*, *HYOU1*, *MANF* and *HSPA5*
366 (Fig. S8C).
367
368 These data suggest that IRE1 controls specific homeostatic programs that
369 prepare the ER and the secretory pathway to match particular physiological needs.
370 These programs address fluctuations in ER function resulting from upsurges in ER
371 protein-folding demands (UPR) or a reduction in ER protein influx upon co-translational
372 translocation deficits (TRES).
373
374 **Discussion**
375
376 IRE1 is known for its two detection and response modes to deviations from ER
377 homeostasis that are triggered by ER protein folding perturbations and lipid bilayer

378 stress, respectively. Here, we describe a hitherto third mode for IRE1 activation dubbed
379 TRES: the sensing and responding to co-translational translocation deficits. Despite
380 lowering the ER's protein-folding burden akin to RIDD and RIDDLE, disrupted co-
381 translational translocation and the subsequent reduction in ER protein influx imbalances
382 the ER's protein folding load and capacity. Fluctuations in protein synthesis, and
383 consequently, oscillations in co-translational translocation occur, for example, during the
384 maturation of B cells into antibody-producing plasma cells (*62*) and during normal
385 functions of the endocrine pancreas, which are notably mediated by the ISR (*63*).
386 Indeed, IRE1 and a primary product resulting from its activation, XBP1s, are essential to
387 maintain the optimal secretory function of these cell types (*32*, *64*, *65*). We propose that
388 a properly balanced ER function is defined by a "Goldilocks zone" in which homeostasis
389 is optimized to the physiological needs of the cell. Displaying a U-shaped response to
390 imbalances on either side, IRE1 emerges as the key ER homeostasis sentinel (Fig. 5,
391 inset).
392
393 *IRE1 follows distinct activation modes in response to ER stress resulting from ER*
394 *overloading and underloading.*
395
396 Our observations support distinct IRE1 activation modes in response to
397 fluctuations in ER load versus capacity, i.e., deviations from homeostasis. In one
398 activation mode, increases in ER protein load cause BiP to dissociate from IRE1,
399 enabling unfolded protein ligands in the ER lumen to bind to IRE1's lumenal domain.
400 Unfolded protein accumulation in the ER lumen promotes IRE1 oligomerization without
401 dissociation from the translocon (see Fig. 1E, compares lanes 2 and 3), possibly by
402 templated and spatially restricted IRE1 self-association. In contrast to this model, it has
403 been proposed that IRE1's association with the translocon regulates the attenuation of
404 its signaling output (*10*, *48*). How IRE1 escapes attenuation imposed by SEC61 binding
405 during unfolded protein stress remains an unresolved question.
406
407 During TRES, co-translational translocation deficiencies result in empty
408 translocons that are conformationally distinct from those in an open state (*66*–*69*). We

409 propose that the closure of the SEC61 channel evicts, and consequentially,
410 derepresses IRE1 (Fig. 5). Our observations that disrupting co-translational
411 translocation by inhibiting the channel, blocking translation initiation, or depleting SRP,
412 induce *XBP1* mRNA splicing bolster this interpretation (Figs.1-3) and support a brake-
413 release model for IRE1 activation upon dissociation from the translocon. Our findings
414 are also consistent with earlier observations, indicating that depleting SEC61 translocon
415 subunits activates IRE1 (*12*).
416
417 *IRE1 activation by TRES is unconventional and defined by specific characteristics.*
418
419 IRE1 activation in response to co-translational translocation defects has three
420 unique characteristics: (i) it is independent of IRE1's conventional ER stress sensing
421 capabilities (Figs. 1-3), (ii) it sidesteps formation of large high-order oligomers visible as
422 foci (Figs. S3, S4H, S6M), and (iii) it is muted in proportion to stress elicited by unfolded
423 protein accumulation (Figs. 1C-D, 2D, 2F - compare lanes 3 and 5, 3K). TRES does not
424 require IRE1's lumenal domain or its transmembrane stress sensing domain. However,
425 the lumenal domain amplifies signaling during TRES, perhaps due to the increased
426 oligomerization potential of the intact protein. TRES activation of IRE1 does not result in
427 formation of visible foci and is lower in magnitude compared to that observed in Tm-
428 induced ER stress. Therefore, substantial *XBP1* mRNA splicing activity can result in the
429 absence of visible foci. It is possible that as stress progresses to an irresolvable state
430 (as would occur with Tm), continued IRE1 self-association leads to the larger
431 assemblies that may be a preamble for IRE1 disposal by degradative means.
432
433 The proportionally muted response of TRES suggests IRE1 is less sensitive to
434 co-translational translocation defects than to unfolded protein accumulation. The vast
435 excess of translocons over IRE1 (back-of-the-envelope calculations indicated by
436 ~2,000-fold (*70*)) implies that IRE1 may sample a specialized subpopulation of
437 translocons dedicated to challenging ER clients. This notion is supported by our
438 previous finding that IRE1 preferentially associates with mRNAs encoding

439 transmembrane proteins (*9*). Distinct translocon-associated factors could confer such
440 specificity (*71*, *72*).
441
442 *IRE1 regulates different outputs in response to ER overload or underload.*
443
444 The distinct IRE1-dependent gene expression programs induced by UPR or
445 TRES activation (Fig. 4) suggest that IRE1 activation modes are tuned to distinct
446 physiological needs to reestablish homeostasis. The tuning can be achieved by
447 combinatorial regulation via transcription factors. The UPR involves cooperation
448 between XBP1s and ATF6-N (the cleaved nuclear form of ATF6, containing its
449 transcription factor moiety) to induce gene expression programs (*27*, *60*) that mitigate
450 ER overload. Conversely, TRES rebalances an underloaded ER by inducing XBP1s
451 alone. ATF6/XBP1s heterodimers and XBP1s homodimers bind to distinct *cis*-regulatory
452 elements, resulting in varied gene expression programs (*29*, *73*). In support of this
453 notion, depleting SEC61 components, SRP machinery, eIF2 subunits, and eIF2B
454 subunits—all of which disrupt co-translational translocation and hinder ER protein
455 import—activates an XBP1s transcriptional reporter built with XBP1s-responsive *cis*-
456 acting elements (*12*). It is also possible that XBP1s partners with other, yet-to-be-
457 identified, transcription factors induced by TRES to induce a tailored gene expression
458 program.
459
460 *TRES is integral to the ISR.*
461
462 TRES links IRE1 activity to the cell-wide attenuation of protein synthesis resulting
463 from the diminished translation initiation that occurs upon eIF2 phosphorylation. Thus,
464 TRES may fulfill an anticipatory role: IRE1 activation downstream of the ISR may
465 prepare the cell for an incoming flux of secretory cargo once the ISR terminates and
466 protein synthesis is restored. Other processes leading to decreased protein synthesis
467 do not have the same impact on IRE1 activation, as indicated by experiments with the
468 elongation inhibitors CHX and EME (Fig. S5C), which freeze ribosomes on their
469 respective mRNAs and hence do not empty translocons. In this case, stalled ribosomes

470 docked onto occupied translocons do not lead to IRE1 eviction from the translocon,
471 preventing its activation. Thus, translational regulation by other means that stabilize
472 existing polysomes would not engage TRES, while we predict that mechanisms that
473 destabilize polysomes will activate it.
474
475 *TRES has pathophysiological implications.*
476
477 Mutations in *SEC63*, which encodes a protein that associates with the
478 translocon, are linked to autosomal dominant polycystic liver disease (ADPLD), a
479 genetic disease characterized by the formation of hepatic cysts, causing organ failure
480 (*74*). Deletion of *Sec63* in mice, which recapitulates cyst formation in the kidney and
481 liver, selectively activates IRE1 (*75*). In support of our findings on the homeostatic
482 nature of IRE1 activation by TRES, *Xbp1* depletion in these mice exacerbates cyst
483 formation while *Xbp1s* overexpression mitigates the disease (*75*). Moreover, IRE1
484 activation by TRES may have a role in oncological indications. For example, a SEC61
485 inhibitor (KZR-261) and Zotatifin are currently in clinical trials for advanced malignant
486 solid tumors (NCT05047536 and NCT04092673), and Zotatifin is in clinical trials for
487 estrogen receptor–positive HER2–negative breast cancer (NCT05101564) and low-
488 grade serous ovarian cancer (NCT03675893). Considering IRE1's adaptive roles and
489 the dependence of some cancers on IRE1 activity (*7*), our results may inform on the
490 therapeutic efficacy (or lack thereof) of targeting co-translational translocation in
491 conjunction with IRE1 modulation to treat cancers. Importantly, given that dysregulation
492 of the ISR is prominently linked to neurodegeneration (*38*), and the ISR inhibitors
493 fosigotifator and DNL343 are in clinical trials (NCT05757141; NCT04948645;
494 NCT06618118; NCT04297683; NCT05842941), it remains to be determined whether
495 IRE1 activity is modulated in these conditions, and if targeting it would have additional
496 therapeutic benefits. Taken together, the discovery of a third modality of IRE1 activation
497 significantly expands our understanding of ER stress in physiology and pathology.
498
499 **Main Text Figure Legends**
500

501 **Figure 1. Disrupted ER translocation activates IRE1.** (A) Schematic representation
502 of the different IRE1 constructs used in this study. Solid red triangle (a.a. E434-D443):
503 translocon association motif; orange dot: W457A. Each doxycycline-inducible transgene
504 was inserted as a single copy using the Flp-In system in U-2 OS *IRE1α*$^{-/-}$ cells. (B) RT-
505 PCR of *XBP1* and *GAPDH* mRNAs (top), immunoblotting of IRE1α, and vinculin (VCL)
506 (bottom) in lysates obtained from U-2 OS *IRE1α*$^{-/-}$ cells expressing mNeonGreen-tagged
507 IRE1α^{WT} and IRE1α^{TAD} upon addition of 5 ng/mL doxycycline (Dox). Cells were treated
508 with 5 µg/mL tunicamycin (Tm) for the indicated times. u - unspliced; s - spliced *XBP1*
509 mRNA amplicons, respectively. The asterisk indicates a hybrid amplicon generated by
510 annealing of one strand of *XBP1u* and one strand of *XBP1s* during the PCR. *GAPDH*,
511 VCL: loading controls. Quantification of the percentage of *XBP1* mRNA splicing is
512 shown in Fig. S1F. Data are representative of three independent experiments. (C) RT-
513 PCR and immunoblots in lysates obtained from U-2 OS *IRE1α*$^{-/-}$ cells expressing
514 mNeonGreen-tagged IRE1α^{DAB} and IRE1α^{BTAD} upon addition of 5 ng/mL Dox. Cells
515 were treated with 5 µg/mL Tm for 4 hours where indicated. Quantification of the
516 percentage of *XBP1* mRNA splicing is shown in Fig. S1G. Data are representative of
517 three independent experiments. (D) RT-PCR and immunoblots in lysates obtained from
518 U-2 OS *IRE1α*$^{-/-}$ cells expressing mNeonGreen-tagged IRE1α^{WT} and IRE1α^{DAB} upon
519 addition of 5 ng/mL doxycycline (Dox). Cells were treated with SEC61-IN-1 for 16 hours
520 at the indicated concentrations. Quantification of the percentage of *XBP1* mRNA
521 splicing is shown in Fig. S2A. Data are representative of three independent
522 experiments. (E) Immunoprecipitation of mNeonGreen-tagged IRE1α^{WT} in U-2 OS
523 *IRE1α*$^{-/-}$ cells expressing IRE1α^{WT} upon addition of 5 ng/mL Dox. Cells were treated with
524 5 µg/mL Tm for 6 hours or 1 µM SEC61-IN-1 for 6 and 16 hours as indicated.
525 Immunoblotting was performed using antibodies against SEC61α and IRE1α. Lanes are
526 cropped from images of the same gel. Data are representative of two independent
527 experiments. (F) Immunoblots of phosphorylated and total IRE1α (top) and spliced
528 XBP1 protein and vinculin (bottom) in lysates obtained from U-2 OS *IRE1α*$^{-/-}$ cells
529 expressing mNeonGreen-tagged IRE1α^{WT} upon addition of 5 ng/mL Dox. Cells were
530 treated with CADA for 16 hours at the indicated concentrations. The quantification of the
531 proportion of phosphorylated IRE1 and spliced XBP1 are shown below the

532 immunoblots. Data are representative of two independent experiments. VCL: loading
533 control. (G) RT-PCR of *XBP1* mRNA in H4 cells depleted of *SRP54* by RNA
534 interference. Quantification of the percentage of *XBP1* mRNA splicing is shown in Fig.
535 S2D. Data are representative of three independent experiments. Bottom panel: extent of
536 *SRP54* knockdown measured by RT-qPCR and normalized internally to *GAPDH*. Mean
537 ± SEM expressed as fold change over the levels in mock-transfected controls (N=3).
538
539 **Figure 2. Translation initiation inhibition activates IRE1.** (A) Immunoprecipitation of
540 mNeonGreen-tagged IRE1α^{WT} in U-2 OS *IRE1α*$^{-/-}$ cells expressing IRE1α^{WT} upon
541 addition of 5 ng/mL Dox. Cells were treated with 500 nM RocA for 16 hours as
542 indicated. Immunoblotting was performed using antibodies against SEC61α, RPL9, and
543 IRE1α. Data are representative of two independent experiments. (B) RT-PCR of *XBP1*
544 and *GAPDH* mRNAs (top), immunoblotting of IRE1α, and VCL (bottom) in lysates
545 obtained from U-2 OS *IRE1α*$^{-/-}$ cells expressing mNeonGreen-tagged IRE1α^{WT} upon
546 addition of 5 ng/mL Dox. Cells were treated with RocA for 16 hours at the indicated
547 concentrations or 5 µg/mL Tm for 4 hours. u - unspliced; s - spliced *XBP1* mRNA
548 amplicons, respectively. The asterisk indicates a hybrid amplicon generated by
549 annealing of one strand of *XBP1u* and one strand of *XBP1s* during the PCR. *GAPDH*,
550 VCL: loading controls. Quantification of the percentage of *XBP1* mRNA splicing is
551 shown in Fig. S4B. Data are representative of three independent experiments. (C)
552 Immunoprecipitation of mNeonGreen-tagged IRE1α^{DAB} as in panel A. (D-E) RT-PCR
553 and immunoblotting as in panel B of lysates obtained from U-2 OS *IRE1α*$^{-/-}$ cells
554 expressing mNeonGreen-tagged IRE1α^{DAB} (D), and mNeonGreen-tagged IRE1α^{TAD} (E).
555 Quantification of the percentage of *XBP1* mRNA splicing is shown in Figs. S4C-D. Data
556 are representative of three independent experiments. (F) RT-PCR of *XBP1* and *GAPDH*
557 mRNAs in lysates obtained from U-2 OS *IRE1α*$^{+/+}$ cells and U-2 OS *IRE1α*$^{-/-}$ cells
558 expressing IRE1α^{WT} cells upon addition of 5 ng/mL Dox. Cells were treated with 100 nM
559 RocA for 16 hours or 5 µg/mL Tm for 4 hours as indicated. Data are representative of
560 three independent experiments. (G) Immunoblots of phosphorylated and total IRE1α
561 (top) and spliced XBP1 protein and VCL (bottom) in lysates obtained from U-2 OS
562 *IRE1α*$^{-/-}$ cells expressing mNeonGreen-tagged IRE1α^{WT} upon addition of 5 ng/mL Dox.

563 Cells were treated with RocA for 16 hours at the indicated concentrations or 5 μg/mL
564 Tm for 4 hours as indicated. The quantification of the proportion of phosphorylated IRE1
565 and spliced XBP1 are shown below the immunoblots. Data are representative of three
566 independent experiments. GAPDH: loading control.
567
568 **Figure 3. Synthetic activation of the ISR induces IRE1.** (A) Schematic representation
569 of FKBP-PKR. The homodimerizer is shown in red. The $FKBP^{F36V}$ domain (light blue) is
570 adjoined to the PKR kinase domain (dark blue) by PKR's unstructured linker. (B) Co-
571 immunoprecipitation of IRE1α and SEC61α in lysates obtained from H4 cells expressing
572 FKBP-PKR and treated with the homodimerizer for 16 hours. (C) Immunoblot of IRE1α
573 phosphorylation (IRE1α-P) and RT-PCR of *XBP1* mRNA and *28S* ribosomal RNA in
574 lysates obtained from H4 cells expressing FKBP-PKR and treated with the
575 homodimerizer for the indicated times. Loading control: *28S* ribosomal RNA. Data are
576 representative of five independent experiments. (D) RT-qPCR of *BLOC1S1* and
577 *SCARA3* mRNAs in H4 cells expressing FKBP-PKR and treated with the homodimerizer
578 for 16 hours with or without co-treatment with 10 μM of the IRE1 RNase inhibitor 4μ8C.
579 Data: Mean ± SEM of fold changes normalized to the levels in untreated controls (N≥3).
580 (E) Immunoblot of IRE1α phosphorylation (IRE1α-P) and RT-PCR of *XBP1* and *GFP*
581 mRNAs in lysates obtained from H4 cells expressing $eIF2\alpha^{S51D}$ hosted in a construct
582 that also expresses GFP, for the indicated times. *GFP* mRNA: transfection and loading
583 control. Data are representative of three independent experiments. The ◊ indicates a
584 non-specific band in the immunoblot (top) and * denotes the hybrid *XBP1* amplicon in
585 the RT-PCR (bottom). (F) RT-qPCR of *BLOC1S1* and *SCARA3* mRNAs in H4 cells
586 expressing $eIF2\alpha^{S51D}$ for 16 hours. Data: Mean ± SEM of fold changes normalized to the
587 levels in untreated controls (N = 3). (G) RT-PCR of *XBP1* mRNA and *28S* ribosomal
588 RNA in H4 cells expressing FKBP-PKR and treated with the homodimerizer for 16 hours
589 with or without co-treatment with 800 nM ISRIB. Data are representative of three
590 independent experiments. (H) RT-qPCR of the expression levels of the *BLOC1S1*
591 mRNA in H4 cells expressing FKBP-PKR, treated with the homodimerizer for 16 hours
592 with or without addition of 800 nM ISRIB. Data: Mean ± SEM of fold changes
593 normalized to the respective levels in untreated controls (N = 3). **p-value < 0.01,

594 Student's t-test. (I) Immunoblots of PERK and ATF4 in lysates obtained from H4 cells
595 expressing FKBP-PKR and treated with the homodimerizer for the indicated times and 5
596 μg/ml Tm for 4 hours. Actin: loading control. (J) left panel: RT-qPCR of the *ATF6* mRNA
597 in H4 cells with CRISPRi-mediated knockdown of *ATF6* (sgATF6); right panel: *HSPA5*
598 mRNA in H4 cells expressing FKBP-PKR cells under the following conditions: 2.5 μg/ml
599 Tm for 16 hours, 5 nM Ceapin-A7, and homodimerizer treatment for 16 hours, as
600 indicated, or in cells with CRISPRi-mediated knockdown of ATF6 (sgATF6). For the
601 right panel data: Mean ± SEM of fold changes normalized to the levels in untreated
602 controls. **p-value <0.01, Student's t-test; n.s. - not significant. (K) RT-PCR of *XBP1*
603 and *GAPDH* mRNAs in U-2 OS *IRE1α*$^{-/-}$ cells expressing FKBP-PKR and mNeonGreen-
604 tagged IRE1α^{DAB} treated with 20 ng/mL Dox for 48 hours, 5 μg/mL Tm for 4 hours as
605 indicated, and the homodimerizer for the indicated times. Data are representative of
606 three independent experiments. The asterisk indicates the hybrid *XBP1* amplicon in the
607 RT-PCR.
608
609 **Figure 4. IRE1 controls distinct gene expression programs in response to**
610 **reduced ER protein influx or increased unfolded protein buildup.** (A-B) Bubble
611 plots showing enriched Reactome pathways to which IRE1-dependent transcripts
612 cluster as upregulated in (A) U-2 OS *IRE1α*$^{-/-}$ cells expressing mNeonGreen-tagged
613 IRE1α^{WT} upon addition of 5 ng/mL Dox and treated with 100 nM RocA for 16 hours (log_2
614 FoldChange > 0.5 compared to DMSO controls), and (B) H4 cells with the activation of
615 FKBP-PKR for 16 hours and 24 hours (continuous enrichment test as compared to
616 controls). (C-D) Heatmaps showing log_2FoldChanges of specific transcripts in U-2 OS
617 *IRE1α*$^{-/-}$ cells, U-2 OS *IRE1α*$^{+/+}$ cells, and U-2 OS *IRE1α*$^{-/-}$ cells expressing
618 mNeonGreen-tagged IRE1α^{WT} upon addition of 5 ng/mL Dox. Cells were treated with
619 100 nM RocA for 16 hours as indicated. In parallel, U-2 OS *IRE1α*$^{-/-}$ cells and U-2 OS
620 *IRE1α*$^{+/+}$ cells were treated with Tm for 4 hours. All log_2FoldChanges were calculated in
621 comparison to DMSO controls. The Reactome pathways to which the protein products
622 of the differentially expressed transcripts belong are highlighted on the left of each
623 panel.
624

625 **Figure 5. Model for IRE1 activation by reduced ER protein influx.** *Schematic model:*
626 (1) Co-translational translocation of signal-peptide bearing proteins into the ER
627 facilitates IRE1's association with the SEC61 translocon. These IRE1 species likely co-
628 exist in a dynamic equilibrium. (2) The IRE1-SEC61 complex functions as an internal
629 limiter of IRE1 activity when the ER protein load is optimal (the 'Goldilocks zone' (3) of
630 ER protein load). (4) During TRES, disrupted co-translational translocation and reduced
631 ER protein influx result in the closure of the SEC61 channel and the subsequent
632 eviction of IRE1 from the translocon complex, leading to IRE1's derepression and TRES
633 signaling. (5) IRE1-driven gene expression programs in-turn prepare the cell for
634 increased rates of protein synthesis and translocation into the ER by upregulating
635 components of the co-translational translocation machinery. *Inset:* U-shaped response
636 of IRE1 activity as a function of ER protein load.
637
638 **Acknowledgments**
639
640 We thank the members of the Acosta-Alvear, Walter, and Costa-Mattioli labs for
641 insightful scientific discussions. We thank Dr. Ramanujan Hegde for advice on using
642 SEC61-IN-1, Dr. Pascal Egea for the structural models of SEC61-IN-1 and CADA
643 bound to the SEC61 translocon, and Dr. Rukmini Mukherjee for advice on the lipid
644 bilayer stress experiments. We thank the Genomics Hub at Altos Labs BAI for their
645 assistance with the RNA-sequencing experiments.
646
647 **Author disclosures**
648
649 PW and DAA are co-inventors of ISRIB. A patent is held by the Regents of the
650 University of California that describes ISRIB and its analogs. Rights to the invention
651 have been licensed by UCSF to Calico. All authors affiliated with Altos Labs are option
652 holders or shareholders in Altos Labs, Inc. All other authors declare no competing
653 interests.
654
655 **Author contributions**

Conceptualization: F.Z., A.S., P.W., D.A-A.
Methodology: F.Z., A.S., B.Y., T.L., J.W., R.Y., T.C., R.M., S.T., P.W., D.A-A.
Investigation: F.Z., A.S., B.Y., J.E.C., T.C.
Writing - Original Draft: F.Z., A.S., P.W., D.A-A.
Writing - Review & Editing: All authors
Visualization: F.Z., A.S., B.Y., N.A.D., P.W., D.A-A.
Supervision: F.Z., A.S., S.T., M. C-M., P.W., D.A-A.

Data, code, and materials availability

The data and materials generated in this study are available upon request through material and data transfer agreements with Altos Labs. The RNA sequencing datasets have been deposited to the Gene Expression Omnibus (GEO) server (accession number: GSE323967). All data are available in the main text or the supplementary materials.

Supplementary Materials
Figs. S1 to S8
Materials and Methods

Supplementary Materials for

IRE1 drives a homeostatic response to reduced protein influx into the endoplasmic reticulum

Zappa, Subramanian *et al.*

Corresponding authors: dacostaalvear@walterlab.science, pwalter@walterlab.science.

The PDF file includes:

Figs. S1 to S8
Materials and Methods
References

Supplementary Figure Legends

Figure S1. Functional characterization of IRE1 mutants used in this study. (A) Immunoprecipitation of mNeonGreen-tagged IRE1α^{WT} and IRE1α^{TAD} in lysates obtained from U-2 OS *IRE1α*$^{-/-}$ cells expressing the respective constructs after the addition of 5 ng/mL Dox for 48 hours. Immunoblotting was performed using antibodies against SEC61α and IRE1α. (B-C) RT-PCR of *XBP1* and *GAPDH* mRNAs in lysates obtained from U-2 OS *IRE1α*$^{-/-}$ cells expressing mNeonGreen-tagged IRE1α^{WT} and IRE1α^{DAB} (B) or mNeonGreen-tagged IRE1^{BTAD} (C) upon addition of 5 ng/mL doxycycline (Dox). Cells were treated with 5 µg/mL Tm for 4 hours, 500 µM palmitic acid for 6 hours, or 1 µM CVT-11127 for 24 hours as indicated. u - unspliced; s - spliced *XBP1* mRNA amplicons, respectively. The asterisk indicates a hybrid amplicon generated by annealing of one strand of *XBP1*u and one strand of *XBP1*s during the PCR. GAPDH: loading control. Data are representative of two independent experiments. (D) Immunoblots of IRE1α and tubulin in lysates obtained from U-2 OS (*IRE1α*$^{+/+}$) cells and U-2 OS *IRE1α*$^{-/-}$ cells expressing mNeonGreen-tagged IRE1α^{WT}, IRE1α^{TAD}, IRE1α^{DAB}, and IRE1α^{BTAD} upon addition of 5 ng/mL doxycycline (Dox) for 48 hours (left). Relative protein expression levels of IRE1 were normalized to tubulin and quantified as a fold change of the mean ± SEM over endogenous IRE1α levels (right) (N=3). (E) RT-qPCR of *IRE1α* mRNA levels in lysates obtained from U-2 OS (*IRE1α*$^{+/+}$) cells and U-2 OS *IRE1α*$^{-/-}$ cells expressing mNeonGreen-tagged IRE1α^{WT}, IRE1α^{TAD}, IRE1α^{DAB}, and IRE1α^{BTAD} upon addition of 5 ng/mL doxycycline (Dox) for 48 hours. Relative *IRE1α* mRNA expression levels were normalized internally to the reference gene *GAPDH* and expressed as $\log_2$(fold change) over the levels in U-2 OS (*IRE1α*$^{+/+}$) cells. Data: mean ± SEM (N=6). (F-G) Quantification of *XBP1* mRNA splicing from experiments shown in Fig. 1B (F) and Fig. 1C (G). Data: mean ± SD (N ≥ 2).

Figure S2. Inhibition of co-translational translocation activates IRE1. (A) Quantification of *XBP1* mRNA splicing from experiments shown in Fig. 1D. Data: mean ± SD (N ≥ 2). (B) Molecular docking of SEC61-IN-1 into the structure of the SEC61 translocon, and Cryo-EM structure of CADA bound to the SEC61 translocon (PDB:

733 8DO2). Panels on the right show the zoomed in views of the small molecules occupying
734 the central pore of SEC61α. (C) Immunoblots of XBP1s, Vinculin (VCL) and IRE1α in
735 lysates obtained from U-2 OS cells treated with CADA and SEC61-IN-1 for 16 hours at
736 the indicated concentrations. The quantification of the proportion of spliced XBP1
737 protein is indicated below. Immunoblots for each treatment were processed in parallel
738 on different gels. Data are representative of two independent experiments. (D)
739 Quantification of *XBP1* mRNA splicing from experiments shown in Fig. 1G. Data: mean
740 ± SD (N ≥ 2).
741
742 **Figure S3. SEC61 translocon inhibition does not induce large IRE1 foci.**
743 Representative micrographs of U-2 OS *IRE1α*$^{-/-}$ cells expressing mNeonGreen-tagged
744 IRE1α^{WT} upon addition of 5 ng/mL doxycycline and treated with 1 μM SEC61-IN-1 or 5
745 μg/mL Tm for the indicated times. Arrowheads indicate high-order mNeonGreen-tagged
746 IRE1α foci observable by confocal fluorescence microscopy. Scale bar = 10 μm.
747
748 **Figure S4. Inhibiting translation initiation activates IRE1.** (A) Quantification of
749 ribosome density based on analysis of transmission electron micrographs of ER
750 membranes (shaded in purple) in U-2 OS cells treated with 100 nM RocA for 16 hours.
751 Electron dense ribosome particles are highlighted in blue. Data: Mean ± SEM (N=22
752 micrographs for control and N=17 micrographs for RocA). (B-D) Quantification of *XBP1*
753 mRNA splicing from experiments shown in Fig. 2B, 2D and 2E. Data: mean ± SD (N ≥
754 2). (E) Immunoblots of XBP1s, IRE1α, and Vinculin (VCL) in lysates obtained from U-2
755 OS cells treated with RocA for 16 hours at the indicated concentrations or 5 μg/mL Tm
756 for 4 hours. The quantification of the proportion of spliced XBP1 protein is indicated
757 below the immunoblots. Data are representative of three independent experiments. (F)
758 RT-qPCR of *SCARA3* and *COL6A1* mRNAs in H4 cells treated with 1 μM RocA for 16
759 hours. Expression levels were normalized internally to 28S ribosomal RNA. Values are
760 expressed as fold change over the levels in H4 cells treated with DMSO (indicated with
761 a dashed line). Data: Mean ± SEM (N = 3). (G) U-2 OS cells treated with RocA at the
762 indicated concentrations for 8 hours were subjected to puromycin pulse-chase analyses
763 to assess nascent protein synthesis rates. Immunoblotting of lysates was performed

764 using antibodies to puromycin and VCL. Data are representative of two independent
765 experiments. Lanes were cropped from the same gel. (H) Confocal micrographs of U-2
766 OS *IRE1α*$^{-/-}$ cells expressing mNeonGreen-tagged IRE1α^{WT} upon addition of 5 ng/mL
767 Dox and treated with 100 nM RocA for the indicated times. Data are representative of
768 two independent experiments. Scale bar = 10 μm.
769
770 **Figure S5. Inhibiting co-translational translocation activates IRE1 but not ATF6 or**
771 **PERK.** (A) RT-PCR of *XBP1* mRNA in lysates obtained from H4 cells treated with RocA
772 and silvestrol at the indicated concentrations for 16 hours. u/s unspliced and spliced
773 *XBP1* amplicons, respectively. (B) RT-PCR of *XBP1* and *GAPDH* mRNAs in lysates
774 obtained from liver tissues of mice treated with 1 mg/kg ZTF or 1 mg/kg Tm for 16
775 hours. *GAPDH*: loading control. The percentage of *XBP1* splicing is shown below the
776 RT-PCR gels and represents Mean ± SEM of N = 8 mice per treatment. VHC - vehicle
777 control. (C) RT-PCR of *XBP1* and *GAPDH* mRNAs in lysates obtained from U-2 OS
778 cells treated with cycloheximide (CHX) and emetine (EME) at the indicated
779 concentrations for 16 hours. *GAPDH*: loading control. (D) Immunoblots of GFP-ATF6 in
780 lysates obtained from U-2 OS cells stably expressing ATF6-GFP (top) and PERK in
781 lysates obtained from U-2 OS cells (bottom). Cells were treated with RocA, SEC61-IN-1
782 and CADA at the indicated concentrations for 16 hours, or 1 mM DTT for 1 hour. GFP-
783 ATF6-N: cleaved ATF6 N-terminus. PERK-P: phosphorylated PERK. VCL: loading
784 control. Immunoblots for each treatment were processed in parallel on different gels.
785 Data are representative of two independent experiments.
786
787 **Figure S6. ISR induction activates IRE1.** (A) H4 cells expressing FKBP-PKR and
788 treated with the homodimerizer for the indicated times were subjected to puromycin
789 pulse-chase analyses to assess nascent protein synthesis rates. Immunoblotting was
790 performed using antibodies to puromycin. Ponceau staining: loading control. Data are
791 representative of three independent experiments. (B) RT-PCR of *XBP1* and *GAPDH*
792 mRNAs in U-2 OS *IRE1α*$^{-/-}$ cells expressing FKBP-PKR and mNeonGreen-tagged
793 IRE1α^{WT}. IRE1α^{WT} expression was induced with 20 ng/mL doxycycline (Dox). Cells
794 were treated with 5 μg/mL Tm for 4 hours or the homodimerizer for the indicated times.

795 Data are representative of three independent experiments. (C-D) RT-qPCR of *DNAJB9*
796 (C) and *HSPA5* (D) mRNAs in H4 cells expressing FKBP-PKR and treated with the
797 homodimerizer. Data: Mean ± SEM of fold changes normalized to the levels in
798 untreated controls; N = 4 for (C), and N = 5 for (D). (E) Immunoblots of FLAG-tagged
799 eIF2α^{S51D}, ATF4, GADD34, and GFP in lysates obtained from H4 cells expressing
800 eIF2α^{S51D} hosted in a construct that also expresses GFP for 24 hours. GFP: loading
801 control. (F-G) RT-qPCR of *DNAJB9* (F) and *HSPA5* (G) mRNAs in H4 cells expressing
802 eIF2α^{S51D} hosted in a construct that also expresses GFP for the indicated times. Data:
803 Mean ± SEM of fold changes normalized to the levels in untreated controls (N ≥ 2). (H-I)
804 RT-qPCR of *DNAJB9* (H) and *HSPA5* (I) mRNAs in H4 cells expressing FKBP-PKR and
805 treated with the dimerizer, with or without co-treatment with 800 nM ISRIB, for 16 hours.
806 Data: Mean ± SEM of fold changes normalized to the levels in untreated controls (N =
807 3). *p-value < 0.05, **p-value < 0.01, Student's t-test. (J) RT-PCR of *XBP1* mRNA in H4
808 cells treated with 10 μM BtdCPU with or without co-treatment with 800 nM ISRIB for 24
809 hours. Data are representative of three independent experiments. (K) RT-PCR of *XBP1*
810 mRNA and *28S* ribosomal RNA in HEK-293 cells treated with 5 ng/μl (6.3 μM)
811 oligomycin (OMY) with or without co-treatment with either 10 μM 4μ8C or 800 nM ISRIB
812 for 16 hours. Data are representative of three independent experiments. (L) RT-qPCR
813 of *GRP94* mRNA in H4 cells expressing FKBP-PKR and treated with the homodimerizer
814 for 16 hours. Data: Mean ± SEM of fold changes normalized to the levels in control
815 cells. (M) Confocal micrographs of U-2 OS *IRE1α*$^{-/-}$ cells expressing FKBP-PKR and
816 mNeonGreen-tagged IRE1α^{WT} and treated with 300 nM thapsigargin (Tg) for 4 hours or
817 the homodimerizer for 16 hours (N = 3). Scale bar = 10μm.
818
819 **Figure S7. RNA sequencing reads validate *XBP1* splicing induction by RocA and**
820 **ISR^{ON} treatments.** (A-B) RNA-sequencing based validation of *XBP1* mRNA splicing in
821 (A) U-2 OS *IRE1α*$^{-/-}$ cells, U-2 OS *IRE1α*$^{+/+}$ cells, and U-2 OS *IRE1α*$^{-/-}$ cells expressing
822 mNeonGreen-tagged IRE1α^{WT} upon addition of 5 ng/mL Dox and treated with 100 nM
823 RocA for 16 hours or Tm for 4 hours as indicated; and (B) H4 cells expressing FKBP-
824 PKR and treated with the homodimerizer for the indicated times. Data: Proportion of
825 *XBP1s* (Ratio of counts per million *XBP1* reads).

826

827 **Figure S8. IRE1 regulates a common set of transcripts in response to RocA or**
828 **tunicamycin treatments.** (A-B) Bubble plots showing differentially enriched Reactome
829 pathways to which IRE1-dependent transcripts cluster as upregulated in (A) U-2 OS
830 *IRE1α*$^{-/-}$ cells expressing mNeonGreen-tagged IRE1α^{WT} upon addition of 5 ng/mL Dox
831 and treated with 100 nM RocA for 16 hours (log_2 FoldChange > 0.5 compared to DMSO
832 controls), and (B) H4 cells with the activation of FKBP-PKR for 16 hours and 24 hours
833 (continuous enrichment test as compared to controls). (C) Heatmap showing log_2
834 FoldChanges of common UPR transcripts in U-2 OS *IRE1α*$^{-/-}$ cells, U-2 OS *IRE1α*$^{+/+}$
835 cells, and U-2 OS *IRE1α*$^{-/-}$ cells expressing mNeonGreen-tagged IRE1α^{WT} upon addition
836 of 5 ng/mL Dox. Cells were treated with 100 nM RocA for 16 hours. In parallel, U-2 OS
837 *IRE1α*$^{-/-}$ and U-2 OS *IRE1α*$^{+/+}$ cells were treated with Tm for 4 hours. All log_2
838 FoldChanges are relative to DMSO controls.

839

840 **Materials and Methods**

841

842 **Cell culture, genetic knockdown, transduction, and drug treatments**

843

844 U-2 OS (ATCC HTB-96), H4 (ATCC HTB-148), and HEK-293 (ATCC CRL-1573) cells
845 were cultured in Dulbecco's Modified Eagle Medium (DMEM) supplemented with 10%
846 fetal bovine serum (FBS) and 1X GlutaMax (Gibco). All cell lines used in the study
847 tested negative for Mycoplasma contamination when assayed with the Universal
848 Mycoplasma Detection Kit. The U-2 OS Flp-In *IRE1α*$^{-/-}$ cells were generated as
849 previously described (*41*). The Flp-In system was used to reconstitute U-2 OS *IRE1α*$^{-/-}$
850 cells with mNeonGreen-tagged IRE1α variants. The parental cells were plated in 6-well
851 plates at a density of 17,000 cells/cm^2. The following day, they were co-transfected with
852 1.7 µg of the Flp recombinase expression vector, pOG44 (Thermo Fisher V600520),
853 and 300 ng of pcDNA5/FRT/TO encoding the tagged IRE1α variants (ThermoFisher
854 V652020). Cells with successful integration were selected with 50 µg/mL hygromycin B
855 (Thermo Fisher 10687010). IRE1α expression was induced by addition of doxycycline
856 for a total duration of 36 - 48 hours unless otherwise stated. U-2 OS mNeonGreen-

857 tagged *IRE1α*$^{-/-}$ cells expressing IRE1α^{WT} or IRE1α$^{\Delta I19\text{-}D408+W457A}$ and FKBP-PKR-P2A-
858 iRFP were obtained through lentiviral infection and were sorted using fluorescent-
859 activated cell sorting (FACS). H4 FKBP-PKR and Tet-On eIF2α S51D-expressing cells
860 were generated as previously described (*54*, *55*). H4 cells expressing the CRISPRi
861 machinery (kind gift of Martin Kampman, UCSF) were used to establish the ATF6 KD
862 cell line by transduction with VSV-G pseudotyped lentiviruses encoding three small
863 guide RNAs. The sgRNA sequences were obtained from the human genome-scale
864 CRISPRi library developed by the laboratory of Jonathan Weissman (MIT, Whitehead
865 Institute). Seventy-two hours after infection, the cells were selected with 1 μg/ml of
866 puromycin (Sigma-Alrich). After selection, a sub-clonal population of cells expressing
867 the sgRNAs was sorted using FACS. Transient gene depletion was achieved through
868 RNA interference (RNAi) by transfecting pooled siRNAs (Dharmacon) using
869 Lipofectamine RNAi MAX (Invitrogen) according to the manufacturer's
870 recommendations. Subsequent analyses were conducted 72-96 hours after
871 transfection. All drugs used in this study are listed in Table 1. Drug concentrations and
872 treatment durations are indicated in the main text and figure legends.
873
874 **Table 1. Drugs used in this study**

Drug	**Vendor**	**Catalogue number**	**Resuspension solvent**	**Concentration used (unless otherwise stated)**
SEC61-IN-1 (A317)	MCE	HY-139615	DMSO (dimethyl sulfoxide)	0.01-10 μM
Rocaglamide	MCE	HY-19356	DMSO	1-1000 nM
Cycloheximide	Arcos (Fisher Scientific)	AC357420010	H_2O	0.01-100 μM

Silvestrol	Abcam	ab285419 (lot# GR3431087-2)	DMSO	0.1-1000 nM
Zotatifin	MCE	HY-112163	5% Dextrose in H_2O	1 mg/kg
Puromycin	Thermo Fisher	AAJ61278MC	DMSO	1 - 2 µg/mL
Cyclotriazadisulfonamide (CADA)	Sigma-Aldrich	5343370001	DMSO	0.001-10 µM
AP-20187 (FKBP homodimerizer)	Takara	635058	Ethanol	100 nM
Tunicamycin	Sigma-Aldrich	SML1287	DMSO	5 µg/mL 1 mg/kg
Thapsigargin	Adipogen Life Sciences	AG-CN2-0003	DMSO	300 nM
4µ8C	SelleckChem	S7272	DMSO	30 µM
DTT (Dithiothreitol)	Sigma-Aldrich	D0632	H_2O	1 mM
Trans-ISRIB	Torcis (Fisher Scientific)	5284	DMSO	800 nM
Ceapin-A7	Torcis (Fisher Scientific)	6955/10 (69-551-0)	DMSO	5 µM
Oligomycin	Sigma-Aldrich	O4876	DMSO	25 µM
BTdCPU	MCE	HY-118266	DMSO	10 µM
KIRA 8	CME	1630086-20-2	DMSO	1 µM

Doxycycline	Sigma-Aldrich	D9891	H_2O	5 - 20 ng/mL
CVT-11127	MCE	HY-113638	DMSO	1 μM
Sodium palmitate	Sigma-Aldrich	SLCN0277	0.1 M NaOH	500 μM

875

876 **Puromycylation assay**

877

878 For the experiments in Fig. S4G, U-2 OS cells were treated with 2 μg/ml puromycin for
879 10 minutes, followed by a wash with 1X PBS. The cells were chased with complete
880 medium with or without RocA for 50 minutes, washed with 1X PBS, lysed with RIPA
881 buffer (1% Triton X-100, 20 mM Tris–HCl pH 8.0, 0.1% SDS, 0.05% sodium
882 deoxycholate, 150 mM NaCl, 10 mM Na3VO4, 40 mM β-glycerophosphate and 10 mM
883 NaF), and the lysates subjected to immunoblotting. For the experiments in Fig. S6A, H4
884 cells were grown to ~70% confluency and incubated with 1 μg/ml puromycin for 20
885 minutes at 37 °C in complete media. After three washes with 1X PBS, the cells were
886 lysed, and the samples were prepared for immunoblotting of puromycylated peptides.

887

888 **Transmission Electron Microscopy (TEM)**

889

890 U-2 OS cells were grown on 35 mm plain-bottom MatTek dishes until they reached ~60-
891 70% confluency, at which point they were fixed in a solution of 3% glutaraldehyde and
892 3% PFA in 1xPBS at pH 7.4 (EMS product 16538-06). Samples were processed for
893 TEM by the Electron Microscope Lab at UC Berkeley, following their standard protocol
894 (https://em-lab.berkeley.edu/EML/tem-generic-protocol). Ultrathin (60 nm) and thick
895 (300 nm) sections were cut by microtome and collected onto formvar-coated copper slot
896 grids. Imaging was performed on a Krios G4 TEM (Thermo Fisher Scientific) operated
897 at 300 kV, equipped with a Selectris X energy filter and a Falcon 4i detector (Thermo
898 Fisher Scientific). Images were acquired at a pixel size of 1-2 nm. Tilt series were
899 collected from -60 to +60 at 2 increments using Tomography 5 software (Thermo Fisher
900 Scientific). The tilt series were processed and reconstructed using TomoLive (Thermo

901 Fisher Scientific), and the 3D reconstructions were analyzed in Amira software (Thermo
902 Fisher Scientific). ER lengths were manually traced and quantified in 2D tomographic
903 slices, and ER-associated ribosomes were manually identified.

904 ***In vivo* studies**

905 All animal procedures were approved by the Altos Labs Institutional Animal Care and
906 Use Committee (IACUC) under protocol 21-105-001. All experiments were conducted
907 strictly with the Guide for the Care and Use of Laboratory Animals (National Research
908 Council, 8th edition) and relevant national regulations. Male C57BL/6J mice (The
909 Jackson Laboratory, Bar Harbor, ME, USA; Strain #000664), 9 weeks of age, were used
910 for the study. Animals were housed in individually ventilated cages with *ad libitum*
911 access to a standard chow diet (Teklad Irradiated Global Soy Protein-Free Extruded
912 Rodent Diet, Inotiv cat#2029X) and purified water. The housing environment was
913 maintained on a 12-hour light/dark cycle (lights on at 07:00 AM, lights off at 07:00 PM),
914 with controlled temperature (20-26 °C) and humidity (40-60%). Mice were acclimated to
915 the facility for 1 week before the start of experimental procedures. Animals were
916 randomly assigned to experimental groups. Experimenters were blinded to treatment
917 groups during drug administration, sample collection, and subsequent data analysis.
918 Tunicamycin (Sigma Aldrich Cat no. SML1287) was diluted 1:25 in 150 mM dextrose to
919 achieve a final concentration of 200 µg/mL. Zotatifin (MCE HY-112163) was
920 resuspended in 5% Dextrose in ddH_2O at a final concentration of 200 µg/mL. The
921 solutions were filter-sterilized using a 0.22 µm syringe filter. Animals received a single
922 intraperitoneal (IP) injection of equal volumes of vehicle control or drugs as follows:
923 Tunicamycin vehicle, 150 mM Dextrose in 4% DMSO; Zotatifin vehicle, 5% Dextrose
924 (278 mM Dextrose) via IP injection. At 16 hours post-injection, mice were terminally
925 anesthetized with isoflurane (2% for induction and 1.5% for maintenance), and their
926 livers were collected after a 1X PBS perfusion. Livers were rinsed in ice-cold PBS and
927 flash-frozen in liquid nitrogen before storage at -80 °C until further analysis.

928 **Immunoblotting**

929

930 For experiments in Fig. 1D, 3C, 3E, 3I and S6A, cell lysates were collected directly in
931 Laemmli SDS-PAGE sample buffer (62.5 mM Tris-HCl pH 6.8, 2% SDS, 10% glycerol,
932 and 0.01% bromophenol blue). Lysates were briefly sonicated and supplemented with
933 fresh 5% 2-mercaptoethanol before heat denaturation and separation by SDS-PAGE.
934 Lysates were separated on SDS-PAGE gels and transferred onto nitrocellulose
935 membranes for immunoblotting. Immunoreactive bands were detected by enhanced
936 chemiluminescence using horseradish peroxidase (HRP)-conjugated secondary
937 antibodies.
938
939 For all other experiments, the cells were washed three times with 1X PBS and
940 immediately collected at 4 °C in RIPA lysis buffer containing phosphatase inhibitors (1%
941 Triton X-100, 20 mM Tris–HCl pH 8.0, 0.1% SDS, 0.05% sodium deoxycholate, 150 mM
942 NaCl, 10 mM Na_3VO_4, 40 mM β-glycerophosphate and 10 mM NaF) and complete
943 protease inhibitors (Roche). The detergent-soluble supernatant fractions were
944 immediately processed for SDS-PAGE and immunoblotting. Antibodies are listed in
945 Table 2.
946
947 **Table 2. Antibodies used in this study**
948

Antibody	**SOURCE**	**IDENTIFIER**
IRE1α Dilution: 1:3000	Cell Signaling Technology	Cat# 3294, RRID:AB_823545
Vinculin Dilution 1:5000	Abcam	Cat# ab18058, RRID:AB_444215

GAPDH Dilution: 1:10000	Proteintech	Cat# 60004-1-Ig, RRID:AB_2107436
SEC61α Dilution 1:3000	Cell Signaling Technology	Cat# 14868, RRID:AB_2722736
IRE1α-P Dilution: 1:3000	Kind gift from Avi Ashkenazi, Genentech	(*76*)
XBP1s Dilution: 1:3000	Cell Signaling Technology	Cat# 40435, RRID:AB_2891025
RPL9 Dilution: 1:3000	Proteintech	Cat# 68054-1-Ig, RRID:AB_2918795
GFP 1:3000	Santa Cruz Biotech	Cat# sc-9996, RRID:AB_627695
PERK Dilution: 1:3000	Cell Signaling Technology	Cat# 3192, RRID:AB_2095847

IRE1α-P Dilution: 1:1000	Abcam	Cat# ab124945, RRID:AB_11001365
ATF4 Dilution 1:2000	Cell Signaling Technology	Cat# 11815, RRID:AB_2616025
Actin Dilution: 1:10000	Cell Signaling Technology	Cat# 4967, RRID:AB_330288
Tubulin Dilution: 1:3000	Proteintech	Cat# 66240-1-Ig, RRID:AB_2881629
Puromycin Dilution: 1:3000	Millipore	Cat# MABE343, RRID:AB_2566826
FLAG Dilution: 1:5000	Thermo Fisher	Cat# MA5-48063, RRID:AB_3074506
GADD34 Dilution: 1:1000	Proteintech	Cat# 10449-1-AP, RRID:AB_2168724

GFP Dilution: 1:10000	Invitrogen	Cat# A-11122, RRID:AB_221569

949

950

951 **IRE1α immunoprecipitation**

952

953 U-2 OS *IRE1α*$^{-/-}$ cells expressing mNeonGreen-tagged IRE1α^{WT} or IRE1α mutants upon
954 addition of 5 ng/mL doxycycline for 48 hours, or H4 cells expressing endogenous levels
955 of IRE1α were washed three times in cold 1X PBS and lysed in a buffer containing 50
956 mM TRIS pH = 8, 150 mM NaCl, 1% digitonin, and protease inhibitor by end-to-end
957 rotation for 30 minutes at 4 °C. The supernatant was collected after centrifugation of
958 lysates at 15,000 rpm for 15 min.

959

960 For mNeonGreen-tag affinity mediated immunoprecipitation, 500 µg of clarified lysate
961 was incubated with agarose or magnetic beads coupled to an mNeonGreen nanobody
962 (ChromTek) overnight in a rotary shaker at 4 °C. Beads were then washed three times
963 with a buffer containing 50 mM Tris pH 8, 150 mM NaCl, 0.1% digitonin, and protease
964 inhibitor. Proteins bound to the beads were eluted by boiling the beads in elution buffer
965 (20 µL of buffer containing 50 mM Tris pH 8, 150 mM NaCl, 0.1% digitonin, and
966 protease inhibitor + 10 µL of Laemmli buffer + 2% 2-mercaptoethanol). The eluates
967 were then subjected to SDS-PAGE and immunoblotting.

968

969 For endogenous IRE1α immunoprecipitation from H4 cells, lysates were first pre-
970 cleaned with Protein A sepharose beads (Cytiva Cat no. 95016-992) on a rotating
971 platform for 20 minutes at 4 °C. The samples were centrifuged at 5000 rpm for 5
972 minutes at 4 °C and the supernatant was collected. 500 µg of supernatant was then
973 incubated overnight, rotating at 4 °C, with 2.5 µg of the anti-IRE1α antibody (Cell

974 Signaling Technology). The beads were then washed 3 times with 800 µL of buffer
975 containing 50 mM Tris pH 8, 150 mM NaCl, 0.2% digitonin, and protease inhibitor. The
976 bound proteins were eluted from the beads by adding Laemmli buffer and boiling for 5
977 minutes at 95 °C. The eluates were then subjected to SDS-PAGE and immunoblotting.
978
979 **Live cell imaging**
980
981 Time-lapse imaging was performed on U-2 OS *IRE1α-/-* cells expressing mNeonGreen-
982 tagged IRE1α^{WT}. Imaging was conducted using a Nikon CREST confocal spinning-disk
983 system, equipped with a 40X water-immersion objective. Cells were maintained in a
984 humidified chamber at 37 °C with 5% CO_2 throughout the experiment. Images were
985 acquired every 30 minutes for a total experimental period of 16 hours.
986
987 **RNA extraction, RT-PCR and quantification of *XBP1* mRNA splicing**
988
989 To measure *XBP1* mRNA splicing in Figures 1D, 1G, S1B, S5A-B, 3C, 3E, 3G, 3K, S6B
990 and S6J-K, total RNA was isolated using the RNeasy RNA purification kit (Qiagen) or
991 the Promega Maxwell automated RNA extractor following the manufacturer's
992 recommendations. 1 µg of total RNA was reverse transcribed with SuperScript VILO
993 (Invitrogen) following the manufacturer's recommendations. The resulting cDNA was
994 diluted 1:10 and used as a template and PCR was performed using primers listed in
995 Table 3 and Hot Start Taq DNA polymerase (NEB). The PCR products were separated
996 on 3% TAE-agarose gel.
997
998 To measure *XBP1* mRNA splicing in all other experiments, total RNA was isolated using
999 the Direct-zol™ RNA Miniprep Plus kit (Zymo Research) according to the
1000 manufacturer's protocols. The yield and the purity of RNA were determined by the
1001 spectrophotometer NanoDrop 2000. For RT-PCR analyses, 1 µg of RNA was converted
1002 to cDNA using the QuantiTect Reverse Transcription Kit (Qiagen). The cDNA was
1003 diluted 1:25 in the PCR reaction tube and the PCR was performed using Promega Go
1004 Taq (NEB). *XBP1* mRNA was amplified using the following primer pairs: *XBP1* Forward:

1005 5'-TTACGAGAGAAAACTCATGGCC-3'; *XBP1* Reverse: 5'-
1006 GGGTCCAAGTTGTCCAGAATGC-3'. *GAPDH* mRNA was amplified using the following
1007 primer pairs: *GAPDH* Forward: 5'-ACCACAGTCCATGCCATC-3'; *GAPDH* Reverse: 5'-
1008 TCCACCCTGTTGCTG-3'. The PCR conditions used were as follows: Step 1: 94 °C - 3
1009 minutes; Step 2: 94 °C - 30s; Step 3: 55 °C - 30s; Step 4: 72 °C - 30s; Step 5 - 72 °C - 7
1010 minutes. Steps 2, 3 and 4 were repeated for 35 cycles. The amplified products were
1011 separated on a 3% TAE-agarose gel containing SYBR-Safe dye.
1012
1013 The gels were imaged using a BioRAD ChemiDoc gel apparatus system, and images
1014 were resized to enhance *XBP1*u and *XBP1*s band separation. For quantification, image
1015 analysis was performed using Fiji (ImageJ). Before quantification, background
1016 correction was applied, and a defined Region of Interest (ROI) was selected for each
1017 lane, encompassing all bands (spliced, unspliced, and hybrid - marked as * in the figure
1018 panels). The intensity was calculated for each band, and the percentage of spliced
1019 *XBP1* (*XBP1s*) was determined as follows: [(*XBP1*s + ½ *XBP1*h) / (*XBP1*s + *XBP1*u +
1020 *XBP1*h)] x 100. The *XBP1* hybrid band is a slower-migrating band that represents a
1021 hybrid DNA molecule. One strand of the hybrid is the unspliced (*XBP1*u) and the other
1022 is the spliced (*XBP1*s) form of the transcript, formed during the PCR reaction itself.
1023
1024 **RNA-seq and Bioinformatics Analyses**
1025
1026 *Library preparation*
1027
1028 Libraries were prepared according to the Watchmaker mRNA Library Prep Kits
1029 (Watchmaker Genomics 7BK0001-096) protocol, using 200 ng of RNA input, and
1030 sequenced on a NextSeq 2000 using XLEAP-SBS chemistry.
1031 *Pre-processing and QC*
1032
1033 Raw sequencing data were demultiplexed using bclconvert. RNA-seq FASTQ files were
1034 trimmed, aligned to the human reference genome (GRCh38, v108), and quantified using

1035 the nf-core/rnaseq pipeline with the star_salmon option (v3.12.0). Gene-level length-
1036 scaled counts were used for all downstream analyses.

1037

1038 *Differential gene expression*

1039

1040 Differentially expressed genes (DEGs) between conditions at each time point were
1041 identified within each dataset using the limma-voom framework. Raw length-scaled
1042 counts were filtered to retain genes with a minimum of 10 counts within biological
1043 groups and trimmed-mean of M-value (TMM) normalization factors were calculated.
1044 Empirical Bayes estimates of the prior variances were robustified against outlier genes.
1045 Thresholds of adjusted p-value < 0.05 after Benjamini-Hochberg correction and
1046 absolute log-fold-change > 0 were used to identify differentially expressed genes.
1047 Sample-wise quality weights were estimated and incorporated into the linear modeling
1048 for the FKBP-PKR dataset using the voomWithQualityWeights function.

1049

1050 *Term Enrichment*

1051

1052 Enriched Reactome terms within comparisons were identified using the continuous
1053 CAMERA test in the FKBP-PKR dataset and a hypergeometric test in the RocA dataset
1054 using the kegga function. The background for the hypergeometric test was all genes
1055 that were tested for differential expression. Significant enrichments were identified with
1056 an adjusted p-value < 0.05 after Benjamini-Hochberg correction. To find groups of
1057 significantly enriched terms, we constructed a graph of Jaccard similarities between all
1058 significant terms based on the number of constituent genes, removed edges with
1059 similarities below 0.3, and performed Louvain clustering with a resolution of 1.

1060

1061 *XBP1 splicing*

1062

1063 To quantify XBP1 slicing (*XBP1s*) levels, salmon was run with 100 bootstraps for each
1064 sample, and transcript-level overdispersion parameters associated with quantification
1065 uncertainty were estimated using the catchSalmon function in edgeR. Raw counts were

1066 corrected for overdispersion, transcripts with fewer than 10 counts across biological
1067 groups were removed, and TMM normalization factors were calculated. Counts-per-
1068 million (CPM) were calculated per sample, and slicing levels were measured as ratios of
1069 CPMs between XBP1s (ENST00000344347) and the sum of all annotated Ensembl
1070 XBP1 transcripts.
1071
1072 **RT-qPCR analyses**
1073
1074 Total RNA from sub-confluent H4 cells or from U-2 OS cells was isolated using the
1075 RNeasy RNA purification kit (Qiagen) or the Promega Maxwell automated RNA
1076 extractor following the manufacturer's recommendations. 1 µg of total RNA was reverse
1077 transcribed with SuperScript VILO (Invitrogen) following the manufacturer's
1078 recommendations. The resulting cDNA was diluted 1:10 and used as a template for
1079 qRT-PCR using PowerUp SYBR Green Master Mix (Applied Biosystems) according to
1080 the manufacturer's protocol. *GAPDH*, *ACTIN*, or 28S rRNA was used as a normalizing
1081 control to estimate fold changes in mRNA expression.
1082
1083 **Table 3. Primers used in this study**
1084

Target	Primer sequence (Fwd)	Primer sequence (Rev)
IRE1	5'-AATGCACACGGCAAGATCA-3'	5'-GAACGGGTGTTTGAGCACG-3'
GAPDH	5'-ACCACAGTCCATGCCATC-3'	5'-TCCACCCTGTTGCTG-3'
28S rRNA	5'-CTTACCAAAAGTGGCCCACTA-3'	5'-AAACTCTGGTGGAGGTCCGT-3'
BLOC1S1	5'-AGCTGGACCATGAGGTGAAG-3'	5'-CTGCAGCTGCCCTTTGTAG-3'

SCARA3	5'-CACATAACTGGGACCAGAGGA-3'	5'-CCTGAAATCGAAAGTATGTTTGG-3'
COL6A1	5'-CTGGGCGTCAAAGTCTTCTC-3'	5'-ATTCGAAGGAGCAGCACACT-3'
GRP94	5'-TGCCAAGGAAGGAGTGAAGT-3'	5'-TCTCCATGTTGCCAGACCAT-3'
GFP	5'-AGCTGTTCACCGGGGTG-3'	5'-GCTGAAGCACTGCACGCC-3'
XBP1	5'-GGAGTTAAGACAGCGCTTGG-3'	5'-ACTGGGTCCAAGTTGTCCAG-3'
SRP54	5'-ACTTCTTGGTATGGGCGACA-3'	5'-AAGATCTGACTGAAGGGGCC-3'
HSPA5	5'-CTATTGGGGTGTTTCGCGAG-3'	5'-GAGAGCTTCATCTTGCCAGC-3'
DNAJB9	5'-ACACTGGATCCAAGAAGCGT-3'	5'-TTGAGTGACAGTCCTGCAGT-3'
ATF6	5'-CCTGCTGTTACCAGCTACCAC-3'	5'-CCAAAGAAGGTGTTGGTTTGA-3'
Mouse XBP1	5'-GGTTGAGAACCAGGAGTTAAGAAC-3'	5'-CTCAGAATCTGAAGAGGCAACAG-3'

Mouse GAPDH	5'-CATTGTCATACCAGGAAATG-3'	5'-GGAGAAACCTGCCAAGTATG-3'

1085

1086 **Molecular docking of SEC61-IN-1 into the SEC61 translocon**

1087

1088 The compatibility of SEC61-IN-1 (SEC61-IN-1/A317) to fit into the canonical SEC61
1089 inhibitor site (*49*) was assessed using interactive docking by analogy to the existing
1090 compounds ipomoeassin F (PDB ID pdb_0008do1) and eeyarestatin I (pdb_00008do3).
1091 In brief, the protein component of the eeyarestatin I complex was prepared for
1092 simulation in ISOLDE (*77*) by deleting the existing ligand, adding hydrogens, and
1093 restraining the geometry with a web of local distance restraints using the "Isolde restrain
1094 distances" command. SEC61-IN-1 was parameterised for simulation using the GAFF2
1095 force field and placed as a rigid body just outside the binding pocket. The ligand was
1096 then maneuvered into the pocket in an interactive physics-based simulation in implicit
1097 solvent and allowed to settle into position without further restraints. The resulting model
1098 buries approximately 460 $Å^2$ without significant change to the protein coordinates. We
1099 note from existing structures that this site in SEC61 exhibits considerable
1100 conformational flexibility; it is likely that binding of this compound would involve some
1101 further rearrangement of the protein, but we have not attempted to model that here.

1102

1103 **References**

1104

1105 1. G. Blobel, Intracellular protein topogenesis. *Proc. Natl. Acad. Sci. U. S. A.* **77**, 1496–
1106 1500 (1980).

1107 2. R. J. Keenan, D. M. Freymann, R. M. Stroud, P. Walter, The signal recognition
1108 particle. *Annu. Rev. Biochem.* **70**, 755–775 (2001).

1109 3. G. Palade, Intracellular aspects of the process of protein synthesis. *Science* **189**,
1110 347–358 (1975).

1111 4. A. E. Johnson, M. A. van Waes, The translocon: a dynamic gateway at the ER
1112 membrane. *Annu Rev Cell Dev Biol* **15**, 799–842 (1999).

1113 5. P. Walter, D. Ron, The unfolded protein response: from stress pathway to
1114 homeostatic regulation. *Science* **334**, 1081–1086 (2011).

1115 6. T. Radanović, J. Reinhard, S. Ballweg, K. Pesek, R. Ernst, An emerging group of
1116 membrane property sensors controls the physical state of organellar membranes to
1117 maintain their identity. *Bioessays* **40**, e1700250 (2018).

1118 7. D. Acosta-Alvear, J. M. Harnoss, P. Walter, A. Ashkenazi, Homeostasis control in
1119 health and disease by the unfolded protein response. *Nat. Rev. Mol. Cell Biol.* **26**,
1120 193–212 (2025).

1121 8. R. Plumb, Z.-R. Zhang, S. Appathurai, M. Mariappan, A functional link between the
1122 co-translational protein translocation pathway and the UPR. *Elife* **4**, e07426 (2015).

1123 9. D. Acosta-Alvear, G. E. Karagöz, F. Fröhlich, H. Li, T. C. Walther, P. Walter, The
1124 unfolded protein response and endoplasmic reticulum protein targeting machineries
1125 converge on the stress sensor IRE1. *Elife* **7**, e43036 (2018).

1126 10. A. Sundaram, R. Plumb, S. Appathurai, M. Mariappan, The Sec61 translocon
1127 limits IRE1α signaling during the unfolded protein response. *Elife* **6**, e27187 (2017).

1128 11. I.-H. Wu, J. S. Yoon, Q. Yang, Y. Liu, W. Skach, P. Thomas, A role for the
1129 ribosome-associated complex in activation of the IRE1 branch of UPR. *Cell Rep* **36**,
1130 109366 (2021).

1131 12. B. Adamson, T. M. Norman, M. Jost, M. Y. Cho, J. K. Nuñez, Y. Chen, J. E.
1132 Villalta, L. A. Gilbert, M. A. Horlbeck, M. Y. Hein, R. A. Pak, A. N. Gray, C. A. Gross,
1133 A. Dixit, O. Parnas, A. Regev, J. S. Weissman, A Multiplexed Single-Cell CRISPR
1134 Screening Platform Enables Systematic Dissection of the Unfolded Protein
1135 Response. *Cell* **167**, 1867-1882.e21 (2016).

1136 13. K. Yanagitani, Y. Imagawa, T. Iwawaki, A. Hosoda, M. Saito, Y. Kimata, K.
1137 Kohno, Cotranslational targeting of XBP1 protein to the membrane promotes
1138 cytoplasmic splicing of its own mRNA. *Mol Cell* **34**, 191–200 (2009).

1139 14. S. Kanda, K. Yanagitani, Y. Yokota, Y. Esaki, K. Kohno, Autonomous
1140 translational pausing is required for XBP1u mRNA recruitment to the ER via the
1141 SRP pathway. *Proc Natl Acad Sci U S A* **113**, E5886–E5895 (2016).

1142 15. A. Sogawa, R. Komori, K. Yanagitani, M. Ohfurudono, A. Tsuru, K. Kadoi, Y.
1143 Kimata, H. Yoshida, K. Kohno, Signal sequence-triage is activated by translocon
1144 obstruction sensed by an ER stress sensor IRE1α. *Cell Struct Funct* **48**, 211–221
1145 (2023).

1146 16. B. M. Gardner, P. Walter, Unfolded proteins are Ire1-activating ligands that
1147 directly induce the unfolded protein response. *Science* **333**, 1891–1894 (2011).

1148 17. Y. Kimata, Y. Ishiwata-Kimata, T. Ito, A. Hirata, T. Suzuki, D. Oikawa, M.
1149 Takeuchi, K. Kohno, Two regulatory steps of ER-stress sensor Ire1 involving its
1150 cluster formation and interaction with unfolded proteins. *J Cell Biol* **179**, 75–86
1151 (2007).

1152 18. G. E. Karagöz, D. Acosta-Alvear, H. T. Nguyen, C. P. Lee, F. Chu, P. Walter, An
1153 unfolded protein-induced conformational switch activates mammalian IRE1. *Elife* **6**,
1154 e30700 (2017).

1155 19. J. J. Credle, J. S. Finer-Moore, F. R. Papa, R. M. Stroud, P. Walter, On the
1156 mechanism of sensing unfolded protein in the endoplasmic reticulum. *Proc. Natl.*
1157 *Acad. Sci. U.S.A.* **102**, 18773–18784 (2005).

1158 20. A. Bertolotti, Y. Zhang, L. M. Hendershot, H. P. Harding, D. Ron, Dynamic
1159 interaction of BiP and ER stress transducers in the unfolded-protein response. *Nat*
1160 *Cell Biol* **2**, 326–332 (2000).

1161 21. K. Halbleib, K. Pesek, R. Covino, H. F. Hofbauer, D. Wunnicke, I. Hänelt, G.
1162 Hummer, R. Ernst, Activation of the Unfolded Protein Response by Lipid Bilayer
1163 Stress. *Mol Cell* **67**, 673-684.e8 (2017).

1164 22. R. Volmer, K. van der Ploeg, D. Ron, Membrane lipid saturation activates
1165 endoplasmic reticulum unfolded protein response transducers through their
1166 transmembrane domains. *Proc Natl Acad Sci U S A* **110**, 4628–4633 (2013).

1167 23. H. Cho, F. Stanzione, A. Oak, G. H. Kim, S. Yerneni, L. Qi, A. K. Sum, C. Chan,
1168 Intrinsic Structural Features of the Human IRE1α Transmembrane Domain Sense
1169 Membrane Lipid Saturation. *Cell Rep* **27**, 307-320.e5 (2019).

1170 24. H. Yoshida, T. Matsui, A. Yamamoto, T. Okada, K. Mori, XBP1 mRNA is induced
1171 by ATF6 and spliced by IRE1 in response to ER stress to produce a highly active
1172 transcription factor. *Cell* **107**, 881–891 (2001).

1173 25. D. Acosta-Alvear, Y. Zhou, A. Blais, M. Tsikitis, N. H. Lents, C. Arias, C. J.
1174 Lennon, Y. Kluger, B. D. Dynlacht, XBP1 controls diverse cell type- and condition-
1175 specific transcriptional regulatory networks. *Mol Cell* **27**, 53–66 (2007).

1176 26. A.-H. Lee, N. N. Iwakoshi, L. H. Glimcher, XBP-1 regulates a subset of
1177 endoplasmic reticulum resident chaperone genes in the unfolded protein response.
1178 *Mol Cell Biol* **23**, 7448–7459 (2003).

1179 27. K. Yamamoto, T. Sato, T. Matsui, M. Sato, T. Okada, H. Yoshida, A. Harada, K.
1180 Mori, Transcriptional induction of mammalian ER quality control proteins is mediated
1181 by single or combined action of ATF6alpha and XBP1. *Dev Cell* **13**, 365–376 (2007).

1182 28. K. J. Travers, C. K. Patil, L. Wodicka, D. J. Lockhart, J. S. Weissman, P. Walter,
1183 Functional and genomic analyses reveal an essential coordination between the
1184 unfolded protein response and ER-associated degradation. *Cell* **101**, 249–258
1185 (2000).

1186 29. M. D. Shoulders, L. M. Ryno, J. C. Genereux, J. J. Moresco, P. G. Tu, C. Wu, J.
1187 R. Yates, A. I. Su, J. W. Kelly, R. L. Wiseman, Stress-independent activation of

1188 XBP1s and/or ATF6 reveals three functionally diverse ER proteostasis
1189 environments. *Cell Rep* **3**, 1279–1292 (2013).

1190 30. J. Hollien, J. S. Weissman, Decay of endoplasmic reticulum-localized mRNAs
1191 during the unfolded protein response. *Science* **313**, 104–107 (2006).

1192 31. A. Le Thomas, E. Ferri, S. Marsters, J. M. Harnoss, D. A. Lawrence, I. Zuazo-
1193 Gaztelu, Z. Modrusan, S. Chan, M. Solon, C. Chalouni, W. Li, H. Koeppen, J.
1194 Rudolph, W. Wang, T. D. Wu, P. Walter, A. Ashkenazi, Decoding non-canonical
1195 mRNA decay by the endoplasmic-reticulum stress sensor IRE1α. *Nat Commun* **12**,
1196 7310 (2021).

1197 32. N. N. Iwakoshi, A.-H. Lee, P. Vallabhajosyula, K. L. Otipoby, K. Rajewsky, L. H.
1198 Glimcher, Plasma cell differentiation and the unfolded protein response intersect at
1199 the transcription factor XBP-1. *Nat Immunol* **4**, 321–329 (2003).

1200 33. L. Romero-Ramirez, H. Cao, D. Nelson, E. Hammond, A.-H. Lee, H. Yoshida, K.
1201 Mori, L. H. Glimcher, N. C. Denko, A. J. Giaccia, Q.-T. Le, A. C. Koong, XBP1 is
1202 essential for survival under hypoxic conditions and is required for tumor growth.
1203 *Cancer Res* **64**, 5943–5947 (2004).

1204 34. J. H. Lin, H. Li, D. Yasumura, H. R. Cohen, C. Zhang, B. Panning, K. M. Shokat,
1205 M. M. Lavail, P. Walter, IRE1 signaling affects cell fate during the unfolded protein
1206 response. *Science* **318**, 944–949 (2007).

1207 35. J.-P. Upton, L. Wang, D. Han, E. S. Wang, N. E. Huskey, L. Lim, M. Truitt, M. T.
1208 McManus, D. Ruggero, A. Goga, F. R. Papa, S. A. Oakes, IRE1α cleaves select
1209 microRNAs during ER stress to derepress translation of proapoptotic Caspase-2.
1210 *Science* **338**, 818–822 (2012).

1211 36. R. Ghosh, L. Wang, E. S. Wang, B. G. K. Perera, A. Igbaria, S. Morita, K. Prado,
1212 M. Thamsen, D. Caswell, H. Macias, K. F. Weiberth, M. J. Gliedt, M. V. Alavi, S. B.
1213 Hari, A. K. Mitra, B. Bhhatarai, S. C. Schürer, E. L. Snapp, D. B. Gould, M. S.
1214 German, B. J. Backes, D. J. Maly, S. A. Oakes, F. R. Papa, Allosteric inhibition of

1215 the IRE1α RNase preserves cell viability and function during endoplasmic reticulum
1216 stress. *Cell* **158**, 534–548 (2014).

1217 37. H. Nishitoh, A. Matsuzawa, K. Tobiume, K. Saegusa, K. Takeda, K. Inoue, S.
1218 Hori, A. Kakizuka, H. Ichijo, ASK1 is essential for endoplasmic reticulum stress-
1219 induced neuronal cell death triggered by expanded polyglutamine repeats. *Genes*
1220 *Dev* **16**, 1345–1355 (2002).

1221 38. M. Costa-Mattioli, P. Walter, The integrated stress response: From mechanism to
1222 disease. *Science* **368**, eaat5314 (2020).

1223 39. M. Boone, F. Zappa, Signaling plasticity in the integrated stress response. *Front*
1224 *Cell Dev Biol* **11**, 1271141 (2023).

1225 40. S. O'Gorman, D. T. Fox, G. M. Wahl, Recombinase-mediated gene activation
1226 and site-specific integration in mammalian cells. *Science* **251**, 1351–1355 (1991).

1227 41. V. Belyy, N.-H. Tran, P. Walter, Quantitative microscopy reveals dynamics and
1228 fate of clustered IRE1α. *Proc Natl Acad Sci U S A* **117**, 1533–1542 (2020).

1229 42. H. Li, A. V. Korennykh, S. L. Behrman, P. Walter, Mammalian endoplasmic
1230 reticulum stress sensor IRE1 signals by dynamic clustering. *Proc Natl Acad Sci U S*
1231 *A* **107**, 16113–16118 (2010).

1232 43. J. Ogbechi, B. S. Hall, T. Sbarrato, J. Taunton, A. E. Willis, R. C. Wek, R. E.
1233 Simmonds, Inhibition of Sec61-dependent translocation by mycolactone uncouples
1234 the integrated stress response from ER stress, driving cytotoxicity via translational
1235 activation of ATF4. *Cell Death Dis* **9**, 397 (2018).

1236 44. E. Lowe, J. L. Anderl, D. Bade, C. Delgado-Martin, C. Dong, R. A. Fan, Y. Fang,
1237 J. Jiang, H. W. B. Johnson, A. Kempema, P. McGilvray, D. McMinn, B. Millare, T.
1238 Muchamuel, N. Poweleit, Y. Qian, S. Rehan, G. Scapin, A. Sugahara, D. Tranter, B.
1239 Tuch, J. Wang, L. Wang, J. A. Whang, P. Zuno-Mitchell, V. O. Paavilainen, E. Park,
1240 J. Taunton, C. J. Kirk, N. K. Anand, Preclinical characterization of novel multi-client

1241 inhibitors of Sec61 with broad antitumor activity. *J Pharmacol Exp Ther* **392**, 103634
1242 (2025).

1243 45. A. Domenger, C. Choisy, L. Baron, V. Mayau, E. Perthame, L. Deriano, B. Arnulf,
1244 J.-C. Bories, G. Dadaglio, C. Demangel, The Sec61 translocon is a therapeutic
1245 vulnerability in multiple myeloma. *EMBO Mol Med* **14**, e14740 (2022).

1246 46. C. McKibbin, A. Mares, M. Piacenti, H. Williams, P. Roboti, M. Puumalainen, A.
1247 C. Callan, K. Lesiak-Mieczkowska, S. Linder, H. Harant, S. High, S. L. Flitsch, R. C.
1248 Whitehead, E. Swanton, Inhibition of protein translocation at the endoplasmic
1249 reticulum promotes activation of the unfolded protein response. *Biochem J* **442**,
1250 639–648 (2012).

1251 47. KEZAR LIFE SCIENCES, Thiazole derivatives as protein secretion inhibitors
1252 (2020).

1253 48. X. Li, S. Sun, S. Appathurai, A. Sundaram, R. Plumb, M. Mariappan, A Molecular
1254 Mechanism for Turning Off IRE1α Signaling during Endoplasmic Reticulum Stress.
1255 *Cell Rep* **33**, 108563 (2020).

1256 49. S. Itskanov, L. Wang, T. Junne, R. Sherriff, L. Xiao, N. Blanchard, W. Q. Shi, C.
1257 Forsyth, D. Hoepfner, M. Spiess, E. Park, A common mechanism of Sec61
1258 translocon inhibition by small molecules. *Nat Chem Biol* **19**, 1063–1071 (2023).

1259 50. S. Iwasaki, S. N. Floor, N. T. Ingolia, Rocaglates convert DEAD-box protein
1260 eIF4A into a sequence-selective translational repressor. *Nature* **534**, 558–561
1261 (2016).

1262 51. C. Müller, W. Obermann, F. W. Schulte, K. Lange-Grünweller, L. Oestereich, F.
1263 Elgner, M. Glitscher, E. Hildt, K. Singh, H.-G. Wendel, R. K. Hartmann, J. Ziebuhr,
1264 A. Grünweller, Comparison of broad-spectrum antiviral activities of the synthetic
1265 rocaglate CR-31-B (-) and the eIF4A-inhibitor Silvestrol. *Antiviral Res* **175**, 104706
1266 (2020).

1267 52. K. von der Malsburg, S. Shao, R. S. Hegde, The ribosome quality control
1268 pathway can access nascent polypeptides stalled at the Sec61 translocon. *Mol Biol*
1269 *Cell* **26**, 2168–2180 (2015).

1270 53. M. McKenna, R. E. Simmonds, S. High, Mycolactone reveals the substrate-
1271 driven complexity of Sec61-dependent transmembrane protein biogenesis. *J Cell*
1272 *Sci* **130**, 1307–1320 (2017).

1273 54. F. Zappa, N. L. Muniozguren, J. E. Conrad, D. Acosta-Alvear, The integrated
1274 stress response engages a cell-autonomous, ligand-independent, DR5-driven
1275 apoptosis switch. *Cell Death Dis* **16**, 101 (2025).

1276 55. F. Zappa, N. L. Muniozguren, M. Z. Wilson, M. S. Costello, J. C. Ponce-Rojas, D.
1277 Acosta-Alvear, Signaling by the integrated stress response kinase PKR is fine-tuned
1278 by dynamic clustering. *J Cell Biol* **221**, e202111100 (2022).

1279 56. C. Sidrauski, D. Acosta-Alvear, A. Khoutorsky, P. Vedantham, B. R. Hearn, H. Li,
1280 K. Gamache, C. M. Gallagher, K. K.-H. Ang, C. Wilson, V. Okreglak, A. Ashkenazi,
1281 B. Hann, K. Nader, M. R. Arkin, A. R. Renslo, N. Sonenberg, P. Walter,
1282 Pharmacological brake-release of mRNA translation enhances cognitive memory.
1283 *Elife* **2**, e00498 (2013).

1284 57. E. Fessler, E.-M. Eckl, S. Schmitt, I. A. Mancilla, M. F. Meyer-Bender, M. Hanf, J.
1285 Philippou-Massier, S. Krebs, H. Zischka, L. T. Jae, A pathway coordinated by
1286 DELE1 relays mitochondrial stress to the cytosol. *Nature* **579**, 433–437 (2020).

1287 58. X. Guo, G. Aviles, Y. Liu, R. Tian, B. A. Unger, Y.-H. T. Lin, A. P. Wiita, K. Xu, M.
1288 A. Correia, M. Kampmann, Mitochondrial stress is relayed to the cytosol by an
1289 OMA1-DELE1-HRI pathway. *Nature* **579**, 427–432 (2020).

1290 59. T. Chen, D. Ozel, Y. Qiao, F. Harbinski, L. Chen, S. Denoyelle, X. He, N.
1291 Zvereva, J. G. Supko, M. Chorev, J. A. Halperin, B. H. Aktas, Chemical genetics
1292 identify eIF2α kinase heme-regulated inhibitor as an anticancer target. *Nat Chem*
1293 *Biol* **7**, 610–616 (2011).

1294 60. K. Lee, W. Tirasophon, X. Shen, M. Michalak, R. Prywes, T. Okada, H. Yoshida,
1295 K. Mori, R. J. Kaufman, IRE1-mediated unconventional mRNA splicing and S2P-
1296 mediated ATF6 cleavage merge to regulate XBP1 in signaling the unfolded protein
1297 response. *Genes Dev* **16**, 452–466 (2002).

1298 61. C. M. Gallagher, P. Walter, Ceapins inhibit ATF6α signaling by selectively
1299 preventing transport of ATF6α to the Golgi apparatus during ER stress. *Elife* **5**,
1300 e11880 (2016).

1301 62. E. van Anken, E. P. Romijn, C. Maggioni, A. Mezghrani, R. Sitia, I. Braakman, A.
1302 J. R. Heck, Sequential waves of functionally related proteins are expressed when B
1303 cells prepare for antibody secretion. *Immunity* **18**, 243–253 (2003).

1304 63. M. Welsh, N. Scherberg, R. Gilmore, D. F. Steiner, Translational control of insulin
1305 biosynthesis. Evidence for regulation of elongation, initiation and signal-recognition-
1306 particle-mediated translational arrest by glucose. *Biochem J* **235**, 459–467 (1986).

1307 64. A. M. Reimold, N. N. Iwakoshi, J. Manis, P. Vallabhajosyula, E. Szomolanyi-
1308 Tsuda, E. M. Gravallese, D. Friend, M. J. Grusby, F. Alt, L. H. Glimcher, Plasma cell
1309 differentiation requires the transcription factor XBP-1. *Nature* **412**, 300–307 (2001).

1310 65. K. L. Lipson, S. G. Fonseca, S. Ishigaki, L. X. Nguyen, E. Foss, R. Bortell, A. A.
1311 Rossini, F. Urano, Regulation of insulin biosynthesis in pancreatic beta cells by an
1312 endoplasmic reticulum-resident protein kinase IRE1. *Cell Metab* **4**, 245–254 (2006).

1313 66. E. Park, J.-F. Ménétret, J. C. Gumbart, S. J. Ludtke, W. Li, A. Whynot, T. A.
1314 Rapoport, C. W. Akey, Structure of the SecY channel during initiation of protein
1315 translocation. *Nature* **506**, 102–106 (2014).

1316 67. B. Van den Berg, W. M. Clemons, I. Collinson, Y. Modis, E. Hartmann, S. C.
1317 Harrison, T. A. Rapoport, X-ray structure of a protein-conducting channel. *Nature*
1318 **427**, 36–44 (2004).

1319 68. R. M. Voorhees, I. S. Fernández, S. H. W. Scheres, R. S. Hegde, Structure of the
1320 mammalian ribosome-Sec61 complex to 3.4 Å resolution. *Cell* **157**, 1632–1643
1321 (2014).

1322 69. R. M. Voorhees, R. S. Hegde, Structure of the Sec61 channel opened by a signal
1323 sequence. *Science* **351**, 88–91 (2016).

1324 70. M. Y. Hein, N. C. Hubner, I. Poser, J. Cox, N. Nagaraj, Y. Toyoda, I. A. Gak, I.
1325 Weisswange, J. Mansfeld, F. Buchholz, A. A. Hyman, M. Mann, A human
1326 interactome in three quantitative dimensions organized by stoichiometries and
1327 abundances. *Cell* **163**, 712–723 (2015).

1328 71. M. Gemmer, M. L. Chaillet, J. van Loenhout, R. Cuevas Arenas, D. Vismpas, M.
1329 Gröllers-Mulderij, F. A. Koh, P. Albanese, R. A. Scheltema, S. C. Howes, A.
1330 Kotecha, J. Fedry, F. Förster, Visualization of translation and protein biogenesis at
1331 the ER membrane. *Nature* **614**, 160–167 (2023).

1332 72. A. Sundaram, Q. Li, Y. Wan, J. Tang, H. Wu, L. Smalinskaitė, R. S. Hegde, Z. Ji,
1333 R. J. Keenan, Global analysis of translocon remodeling during protein synthesis at
1334 the ER. *Nat Struct Mol Biol*, doi: 10.1038/s41594-025-01691-6 (2025).

1335 73. K. Yamamoto, H. Yoshida, K. Kokame, R. J. Kaufman, K. Mori, Differential
1336 contributions of ATF6 and XBP1 to the activation of endoplasmic reticulum stress-
1337 responsive cis-acting elements ERSE, UPRE and ERSE-II. *J Biochem* **136**, 343–
1338 350 (2004).

1339 74. S. Davila, L. Furu, A. G. Gharavi, X. Tian, T. Onoe, Q. Qian, A. Li, Y. Cai, P. S.
1340 Kamath, B. F. King, P. J. Azurmendi, P. Tahvanainen, H. Kääriäinen, K.
1341 Höckerstedt, O. Devuyst, Y. Pirson, R. S. Martin, R. P. Lifton, E. Tahvanainen, V. E.
1342 Torres, S. Somlo, Mutations in SEC63 cause autosomal dominant polycystic liver
1343 disease. *Nat Genet* **36**, 575–577 (2004).

1344 75. S. V. Fedeles, J.-S. So, A. Shrikhande, S. H. Lee, A.-R. Gallagher, C. E.
1345 Barkauskas, S. Somlo, A.-H. Lee, Sec63 and Xbp1 regulate IRE1α activity and
1346 polycystic disease severity. *J Clin Invest* **125**, 1955–1967 (2015).

1347 76. T.-K. Chang, D. A. Lawrence, M. Lu, J. Tan, J. M. Harnoss, S. A. Marsters, P.
1348 Liu, W. Sandoval, S. E. Martin, A. Ashkenazi, Coordination between Two Branches
1349 of the Unfolded Protein Response Determines Apoptotic Cell Fate. *Mol Cell* **71**, 629-
1350 636.e5 (2018).

1351 77. T. I. Croll, ISOLDE: a physically realistic environment for model building into low-
1352 resolution electron-density maps. *Acta Crystallogr D Struct Biol* **74**, 519–530 (2018).

Figure 1

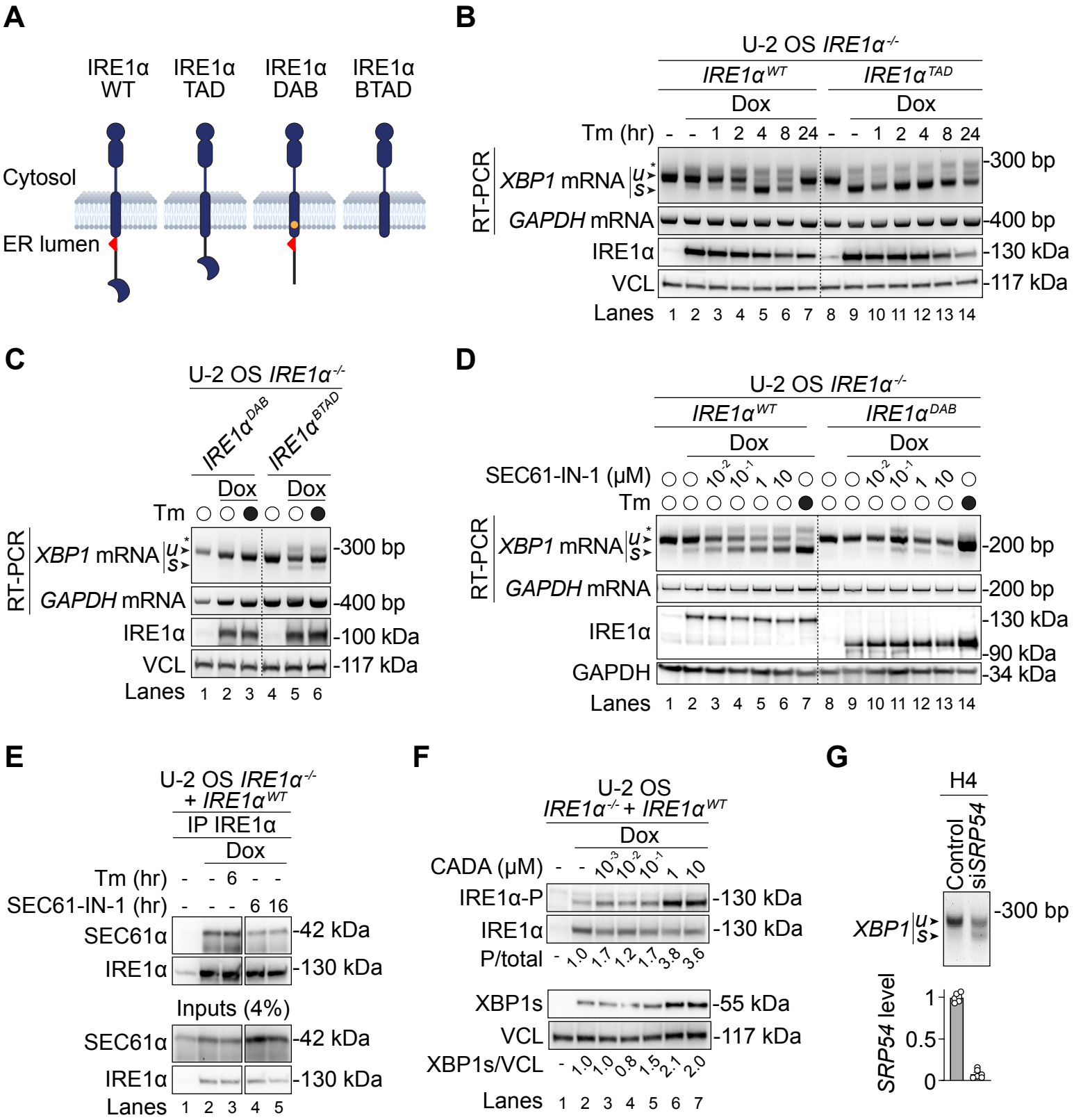
A
IRE1α WT
IRE1α TAD
IRE1α DAB
IRE1α BTAD
Cytosol
ER lumen
B
U-2 OS IRE1α-/-
IRE1αWT
IRE1αTAD
Dox
Tm (hr) - - 1 2 4 8 24 - - 1 2 4 8 24
RT-PCR
XBP1 mRNA
u
s
GAPDH mRNA
IRE1α
VCL
-300 bp
-400 bp
-130 kDa
-117 kDa
Lanes 1 2 3 4 5 6 7 8 9 10 11 12 13 14
C
U-2 OS IRE1α-/-
IRE1αDAB
IRE1αBTAD
Dox
Tm
RT-PCR
XBP1 mRNA
GAPDH mRNA
IRE1α
VCL
-300 bp
-400 bp
-100 kDa
-117 kDa
Lanes 1 2 3 4 5 6
D
U-2 OS IRE1α-/-
IRE1αWT
IRE1αDAB
Dox
SEC61-IN-1 (μM)
10-2 10-1 1 10
Tm
RT-PCR
XBP1 mRNA
GAPDH mRNA
IRE1α
GAPDH
-200 bp
-200 bp
-130 kDa
-90 kDa
-34 kDa
Lanes 1 2 3 4 5 6 7 8 9 10 11 12 13 14
E
U-2 OS IRE1α-/-
+ IRE1αWT
IP IRE1α
Dox
Tm (hr) - - 6 - -
SEC61-IN-1 (hr) - - - 6 16
SEC61α
IRE1α
-42 kDa
-130 kDa
Inputs (4%)
SEC61α
IRE1α
-42 kDa
-130 kDa
Lanes 1 2 3 4 5
F
U-2 OS
IRE1α-/- + IRE1αWT
Dox
CADA (μM) - - 10-3 10-2 10-1 1 10
IRE1α-P
IRE1α
P/total - 1.0 1.7 1.2 1.7 3.8 3.6
-130 kDa
-130 kDa
XBP1s
VCL
XBP1s/VCL - 1.0 1.0 0.8 1.5 2.1 2.0
-55 kDa
-117 kDa
Lanes 1 2 3 4 5 6 7
G
H4
Control
siSRP54
XBP1
u
s
-300 bp
SRP54 level
1
0.5
0

Figure 2

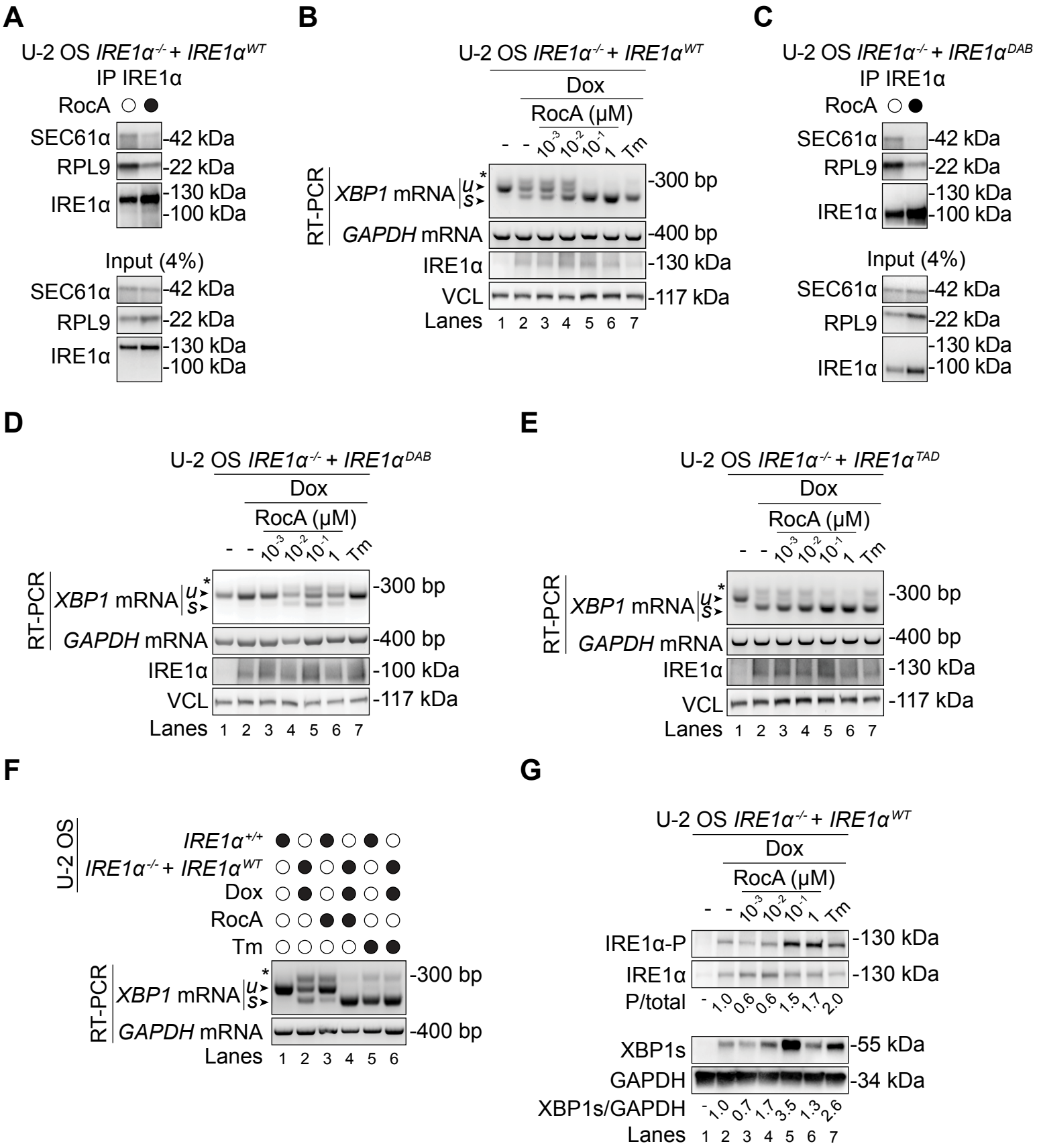
A
U-2 OS IRE1α-/- + IRE1αWT
IP IRE1α
RocA
SEC61α -42 kDa
RPL9 -22 kDa
IRE1α -130 kDa -100 kDa
Input (4%)
SEC61α -42 kDa
RPL9 -22 kDa
IRE1α -130 kDa -100 kDa
B
U-2 OS IRE1α-/- + IRE1αWT
Dox
RocA (μM)
- - 10-3 10-2 10-1 1 Tm
RT-PCR
XBP1 mRNA u s * -300 bp
GAPDH mRNA -400 bp
IRE1α -130 kDa
VCL -117 kDa
Lanes 1 2 3 4 5 6 7
C
U-2 OS IRE1α-/- + IRE1αDAB
IP IRE1α
RocA
SEC61α -42 kDa
RPL9 -22 kDa
IRE1α -130 kDa -100 kDa
Input (4%)
SEC61α -42 kDa
RPL9 -22 kDa
IRE1α -130 kDa -100 kDa
D
U-2 OS IRE1α-/- + IRE1αDAB
Dox
RocA (μM)
- - 10-3 10-2 10-1 1 Tm
RT-PCR
XBP1 mRNA u s * -300 bp
GAPDH mRNA -400 bp
IRE1α -100 kDa
VCL -117 kDa
Lanes 1 2 3 4 5 6 7
E
U-2 OS IRE1α-/- + IRE1αTAD
Dox
RocA (μM)
- - 10-3 10-2 10-1 1 Tm
RT-PCR
XBP1 mRNA u s * -300 bp
GAPDH mRNA -400 bp
IRE1α -130 kDa
VCL -117 kDa
Lanes 1 2 3 4 5 6 7
F
U-2 OS
IRE1α+/+
IRE1α-/- + IRE1αWT
Dox
RocA
Tm
RT-PCR
XBP1 mRNA u s * -300 bp
GAPDH mRNA -400 bp
Lanes 1 2 3 4 5 6
G
U-2 OS IRE1α-/- + IRE1αWT
Dox
RocA (μM)
- - 10-3 10-2 10-1 1 Tm
IRE1α-P -130 kDa
IRE1α -130 kDa
P/total - 1.0 0.6 0.6 1.5 1.7 2.0
XBP1s -55 kDa
GAPDH -34 kDa
XBP1s/GAPDH - 1.0 0.7 1.7 3.5 1.3 2.6
Lanes 1 2 3 4 5 6 7

Figure 3

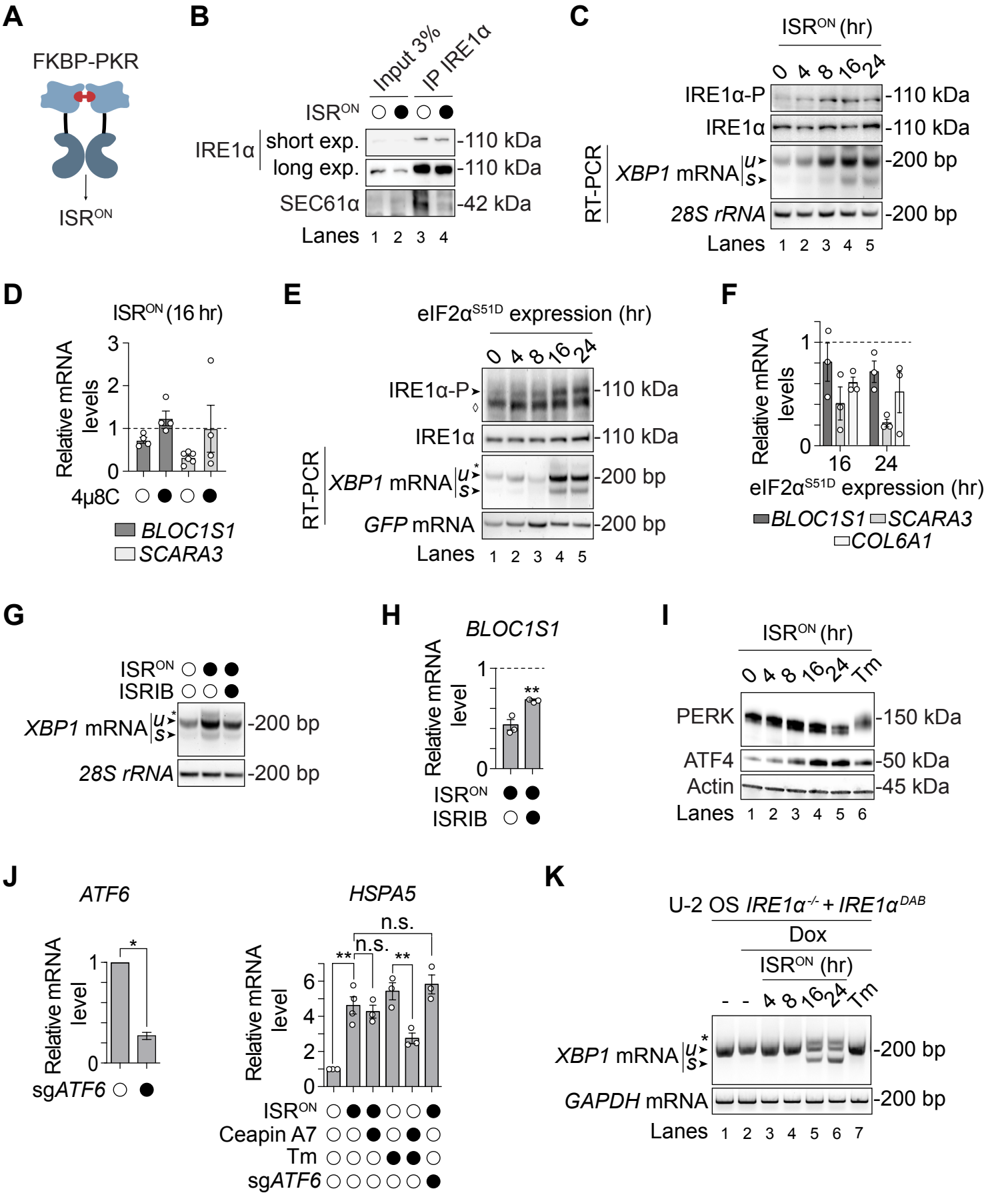
A
FKBP-PKR
ISR^ON
B
Input 3%
IP IRE1α
ISR^ON
IRE1α
short exp.
long exp.
-110 kDa
-110 kDa
SEC61α
-42 kDa
Lanes 1 2 3 4
C
ISR^ON (hr)
0 4 8 16 24
IRE1α-P
IRE1α
-110 kDa
-110 kDa
RT-PCR
XBP1 mRNA
u
s
-200 bp
28S rRNA
-200 bp
Lanes 1 2 3 4 5
D
ISR^ON (16 hr)
Relative mRNA levels
4μ8C
BLOC1S1
SCARA3
E
eIF2α^S51D expression (hr)
0 4 8 16 24
IRE1α-P
IRE1α
-110 kDa
-110 kDa
RT-PCR
XBP1 mRNA
u
s
-200 bp
GFP mRNA
-200 bp
Lanes 1 2 3 4 5
F
Relative mRNA levels
16 24
eIF2α^S51D expression (hr)
BLOC1S1
SCARA3
COL6A1
G
ISR^ON
ISRIB
XBP1 mRNA
u
s
-200 bp
28S rRNA
-200 bp
H
BLOC1S1
Relative mRNA level
ISR^ON
ISRIB
I
ISR^ON (hr)
0 4 8 16 24 Tm
PERK
-150 kDa
ATF4
-50 kDa
Actin
-45 kDa
Lanes 1 2 3 4 5 6
J
ATF6
Relative mRNA level
sgATF6
HSPA5
n.s.
n.s.
Relative mRNA level
ISR^ON
Ceapin A7
Tm
sgATF6
K
U-2 OS IRE1α^-/- + IRE1α^DAB
Dox
ISR^ON (hr)
- - 4 8 16 24 Tm
XBP1 mRNA
u
s
-200 bp
GAPDH mRNA
-200 bp
Lanes 1 2 3 4 5 6 7

Figure 4

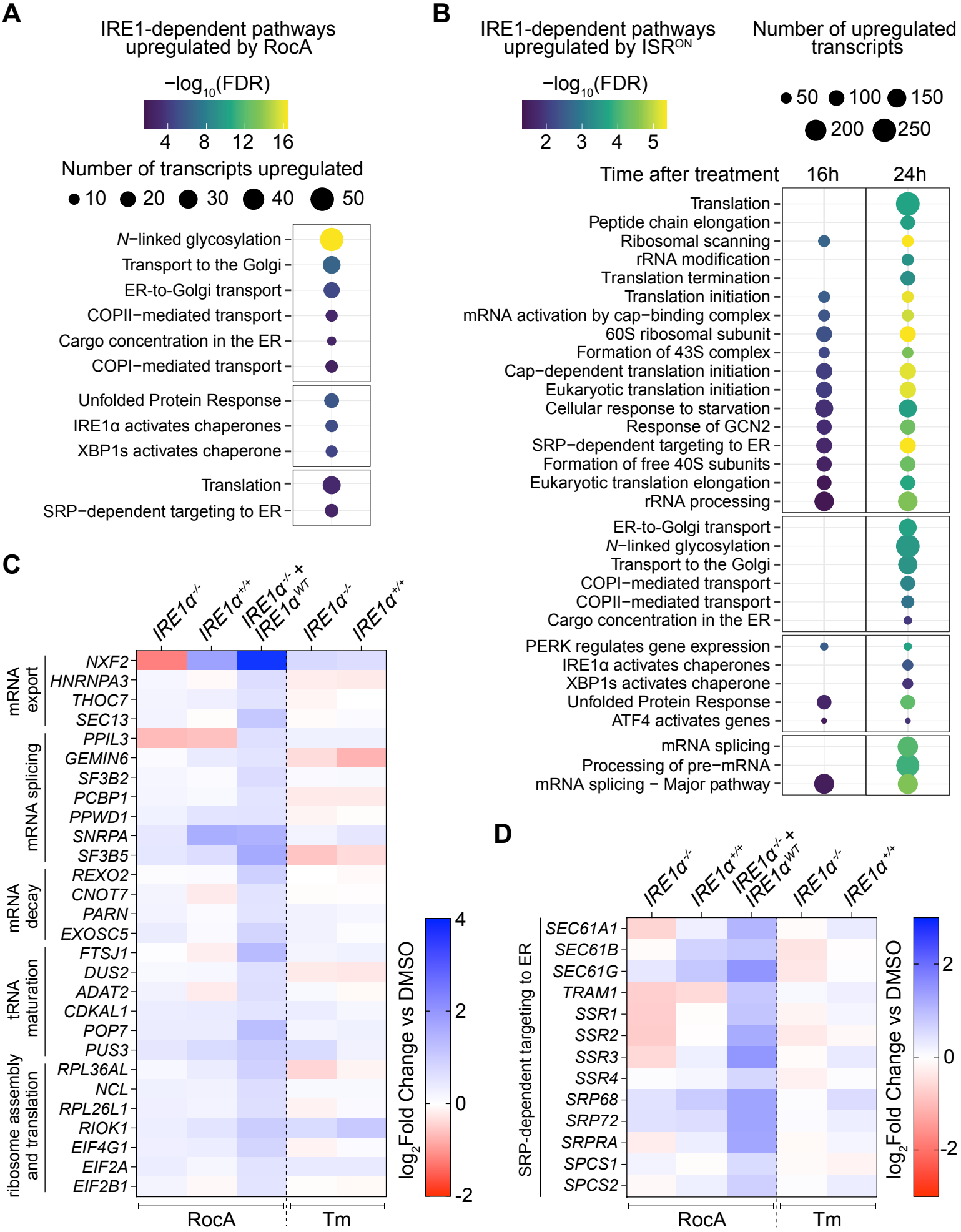
A
IRE1-dependent pathways upregulated by RocA
−log10(FDR)
4 8 12 16
Number of transcripts upregulated
10 20 30 40 50
N−linked glycosylation
Transport to the Golgi
ER-to-Golgi transport
COPII−mediated transport
Cargo concentration in the ER
COPI−mediated transport
Unfolded Protein Response
IRE1α activates chaperones
XBP1s activates chaperone
Translation
SRP−dependent targeting to ER
B
IRE1-dependent pathways upregulated by ISRON
−log10(FDR)
2 3 4 5
Number of upregulated transcripts
50 100 150 200 250
Time after treatment
16h
24h
Translation
Peptide chain elongation
Ribosomal scanning
rRNA modification
Translation termination
Translation initiation
mRNA activation by cap−binding complex
60S ribosomal subunit
Formation of 43S complex
Cap−dependent translation initiation
Eukaryotic translation initiation
Cellular response to starvation
Response of GCN2
SRP−dependent targeting to ER
Formation of free 40S subunits
Eukaryotic translation elongation
rRNA processing
ER-to-Golgi transport
N−linked glycosylation
Transport to the Golgi
COPI−mediated transport
COPII−mediated transport
Cargo concentration in the ER
PERK regulates gene expression
IRE1α activates chaperones
XBP1s activates chaperone
Unfolded Protein Response
ATF4 activates genes
mRNA splicing
Processing of pre−mRNA
mRNA splicing − Major pathway
C
IRE1α−/−
IRE1α+/+
IRE1α−/− + IRE1αWT
IRE1α−/−
IRE1α+/+
mRNA export
NXF2
HNRNPA3
THOC7
SEC13
mRNA splicing
PPIL3
GEMIN6
SF3B2
PCBP1
PPWD1
SNRPA
SF3B5
mRNA decay
REXO2
CNOT7
PARN
EXOSC5
tRNA maturation
FTSJ1
DUS2
ADAT2
CDKAL1
POP7
PUS3
ribosome assembly and translation
RPL36AL
NCL
RPL26L1
RIOK1
EIF4G1
EIF2A
EIF2B1
RocA
Tm
log2Fold Change vs DMSO
4
2
0
-2
D
IRE1α−/−
IRE1α+/+
IRE1α−/− + IRE1αWT
IRE1α−/−
IRE1α+/+
SRP-dependent targeting to ER
SEC61A1
SEC61B
SEC61G
TRAM1
SSR1
SSR2
SSR3
SSR4
SRP68
SRP72
SRPRA
SPCS1
SPCS2
RocA
Tm
log2Fold Change vs DMSO
2
0
-2

Figure 5

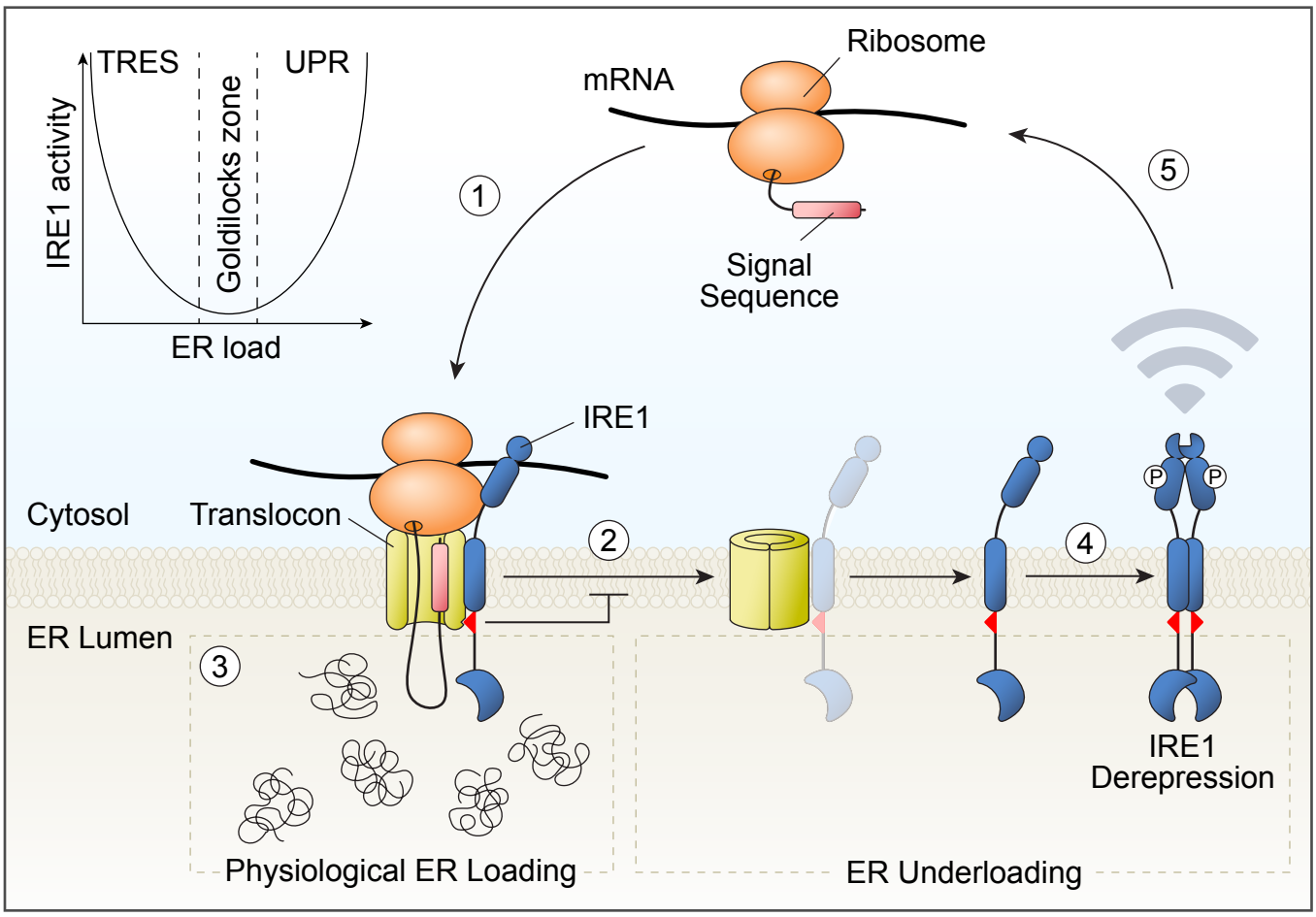
TRES
UPR
Goldilocks zone
IRE1 activity
ER load
Ribosome
mRNA
Signal
Sequence
1
5
IRE1
Cytosol
Translocon
2
4
P
P
ER Lumen
3
IRE1
Derepression
Physiological ER Loading
ER Underloading

Figure S1

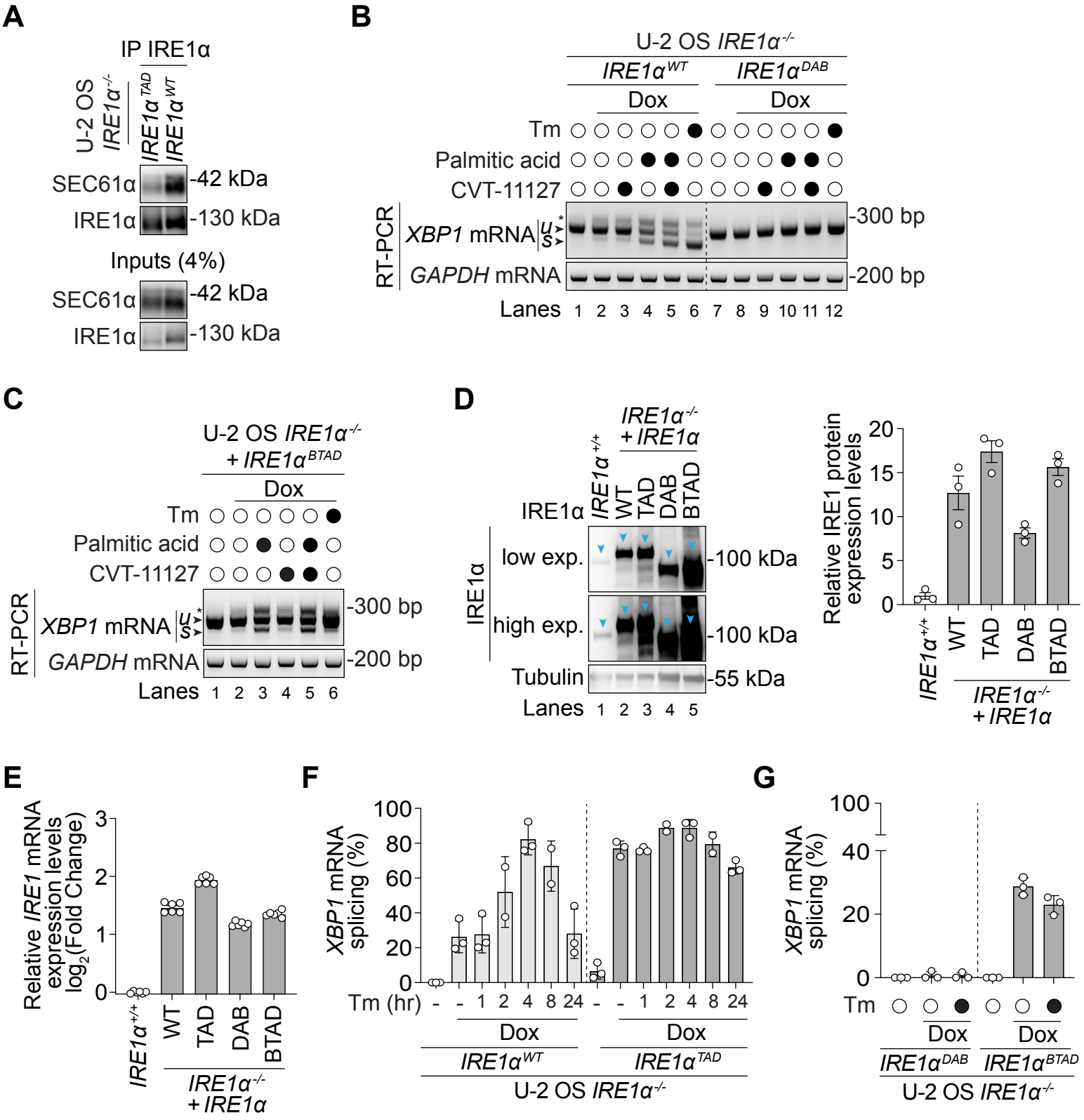
A
IP IRE1α
U-2 OS IRE1α-/-
IRE1α TAD
IRE1α WT
SEC61α
-42 kDa
IRE1α
-130 kDa
Inputs (4%)
SEC61α
-42 kDa
IRE1α
-130 kDa
B
U-2 OS IRE1α-/-
IRE1α WT
IRE1α DAB
Dox
Dox
Tm
Palmitic acid
CVT-11127
RT-PCR
XBP1 mRNA
u
s
-300 bp
GAPDH mRNA
-200 bp
Lanes 1 2 3 4 5 6 7 8 9 10 11 12
C
U-2 OS IRE1α-/-
+ IRE1α BTAD
Dox
Tm
Palmitic acid
CVT-11127
RT-PCR
XBP1 mRNA
u
s
-300 bp
GAPDH mRNA
-200 bp
Lanes 1 2 3 4 5 6
D
IRE1α-/-
+ IRE1α
IRE1α
IRE1α +/+
WT
TAD
DAB
BTAD
IRE1α
low exp.
high exp.
-100 kDa
-100 kDa
Tubulin
-55 kDa
Lanes 1 2 3 4 5
Relative IRE1 protein expression levels
20
15
10
5
0
IRE1α +/+
WT
TAD
DAB
BTAD
IRE1α-/-
+ IRE1α
E
Relative IRE1 mRNA expression levels
log2(Fold Change)
3
2
1
0
IRE1α +/+
WT
TAD
DAB
BTAD
IRE1α-/-
+ IRE1α
F
XBP1 mRNA splicing (%)
100
80
60
40
20
0
Tm (hr) - - 1 2 4 8 24 - - 1 2 4 8 24
Dox
Dox
IRE1α WT
IRE1α TAD
U-2 OS IRE1α-/-
G
XBP1 mRNA splicing (%)
100
40
20
0
Tm
Dox
Dox
IRE1α DAB
IRE1α BTAD
U-2 OS IRE1α-/-

Figure S2

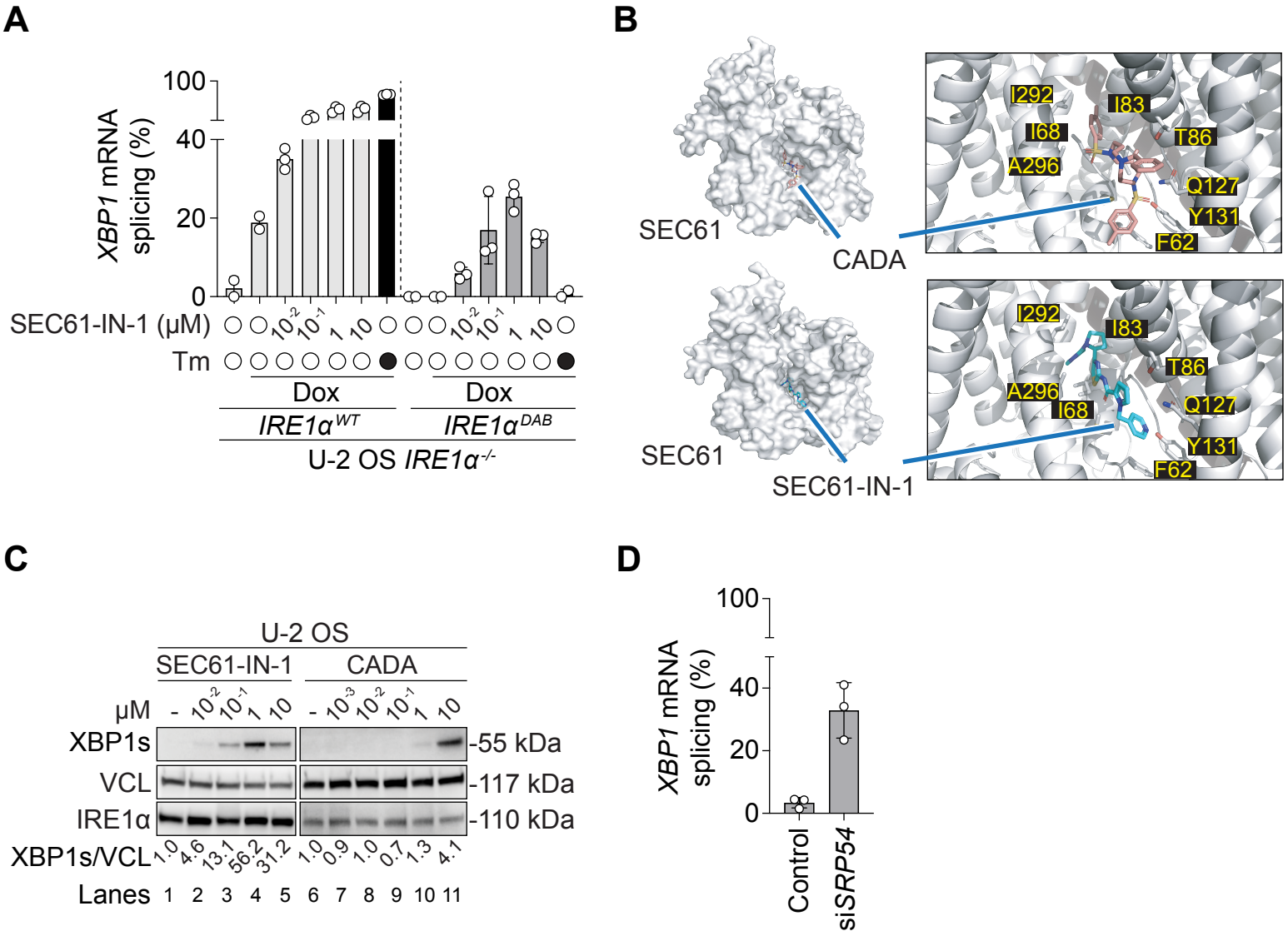
A
XBP1 mRNA splicing (%)
100
40
20
0
SEC61-IN-1 (μM)
10-2
10-1
1
10
Tm
Dox
Dox
IRE1α WT
IRE1α DAB
U-2 OS IRE1α -/-
B
SEC61
CADA
I292
I83
I68
T86
A296
Q127
Y131
F62
SEC61
SEC61-IN-1
C
U-2 OS
SEC61-IN-1
CADA
μM
-
10-3
XBP1s
VCL
IRE1α
-55 kDa
-117 kDa
-110 kDa
XBP1s/VCL
1.0
4.6
13.1
56.2
31.2
0.9
0.7
1.3
4.1
Lanes
1 2 3 4 5 6 7 8 9 10 11
D
Control
siSRP54

Figure S3

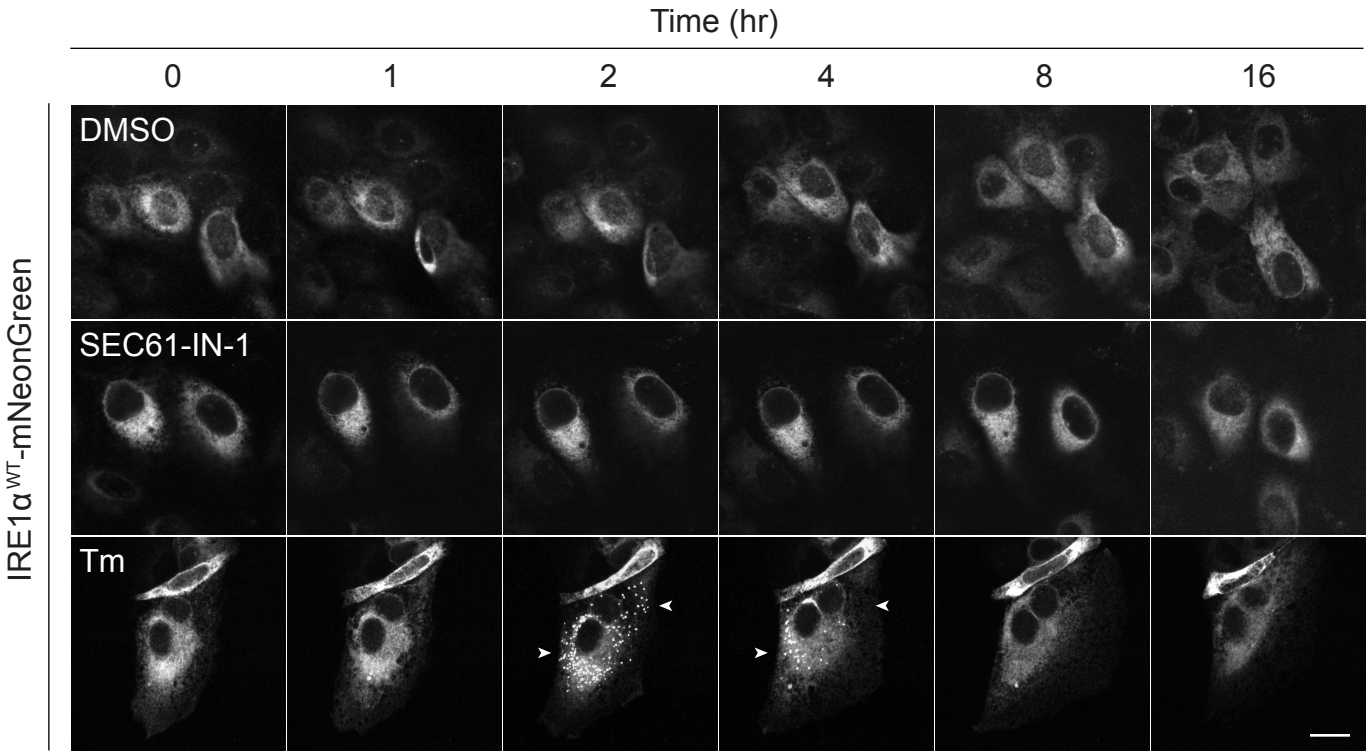

Figure S4

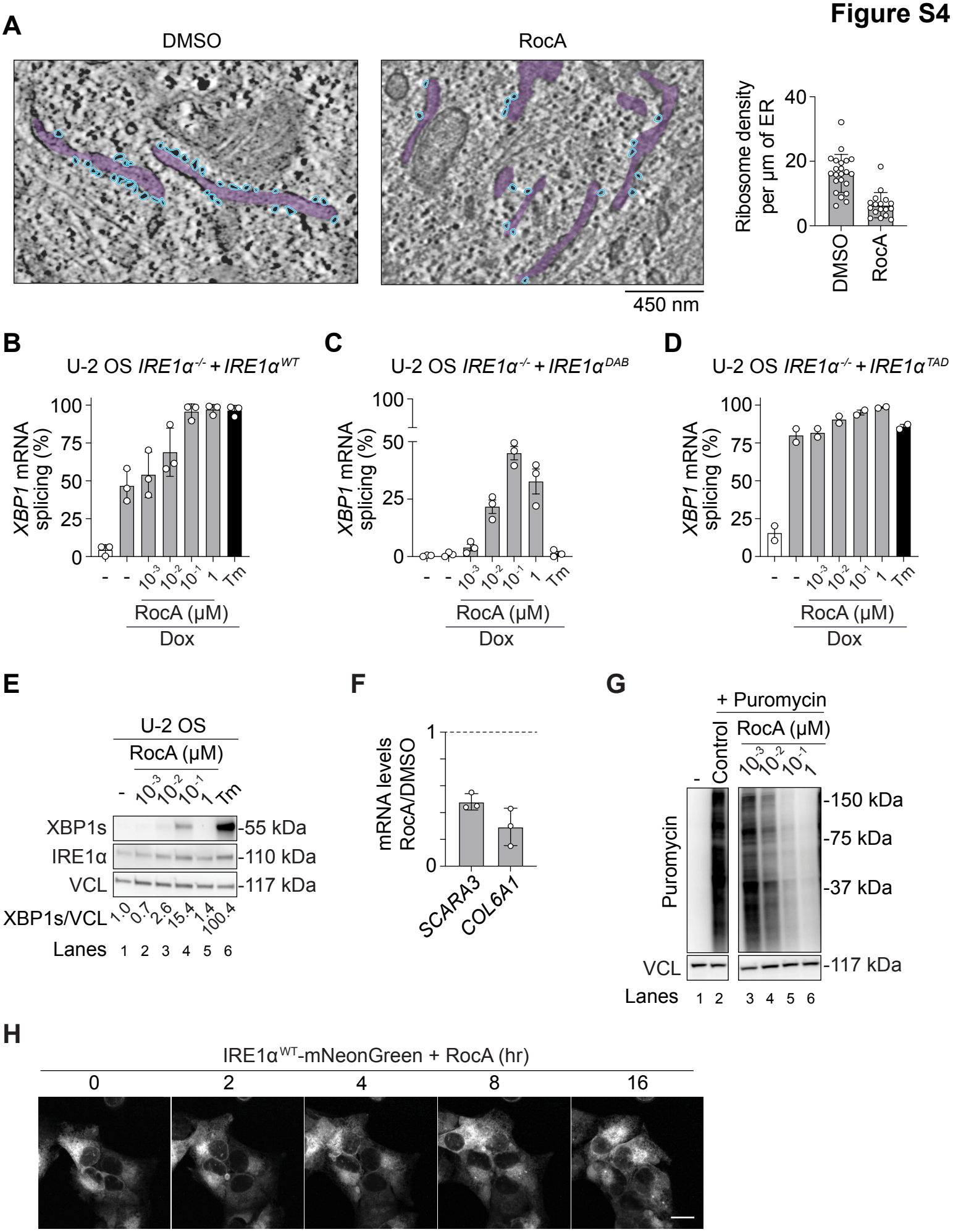
A
DMSO
RocA
450 nm
Ribosome density per µm of ER
40
20
0
DMSO
RocA
B
U-2 OS IRE1α-/- + IRE1αWT
XBP1 mRNA splicing (%)
100
75
50
25
0
- - 10-3 10-2 10-1 1 Tm
RocA (µM)
Dox
C
U-2 OS IRE1α-/- + IRE1αDAB
XBP1 mRNA splicing (%)
100
50
25
0
- - 10-3 10-2 10-1 1 Tm
RocA (µM)
Dox
D
U-2 OS IRE1α-/- + IRE1αTAD
XBP1 mRNA splicing (%)
100
75
50
25
0
- - 10-3 10-2 10-1 1 Tm
RocA (µM)
Dox
E
U-2 OS
RocA (µM)
- 10-3 10-2 10-1 1 Tm
XBP1s
-55 kDa
IRE1α
-110 kDa
VCL
-117 kDa
XBP1s/VCL 1.0 0.7 2.6 15.4 1.4 100.4
Lanes 1 2 3 4 5 6
F
mRNA levels RocA/DMSO
1
0
SCARA3
COL6A1
G
+ Puromycin
Control
RocA (µM)
- 10-3 10-2 10-1 1
Puromycin
-150 kDa
-75 kDa
-37 kDa
VCL
-117 kDa
Lanes 1 2 3 4 5 6
H
IRE1αWT-mNeonGreen + RocA (hr)
0
2
4
8
16

Figure S5

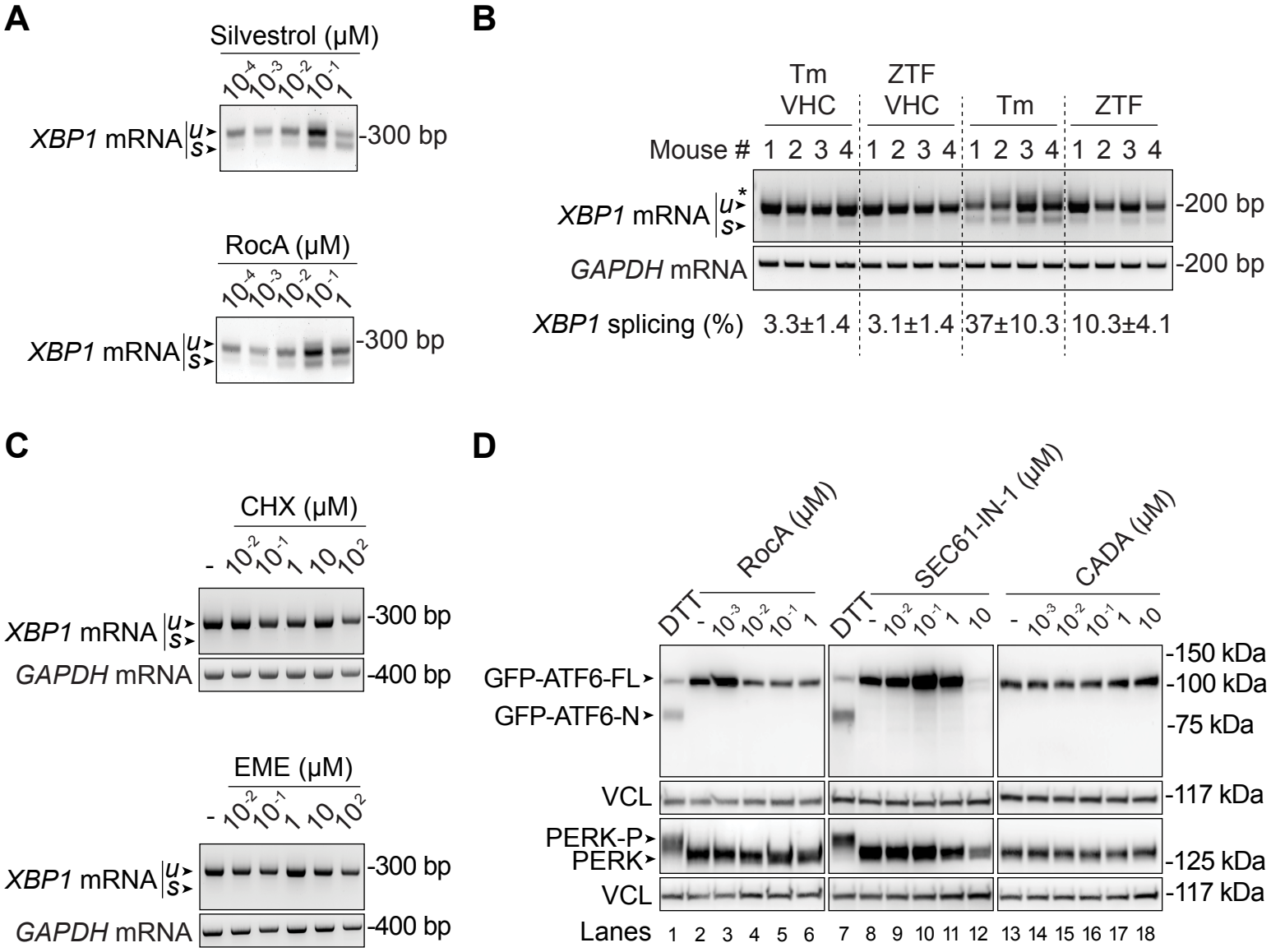
A
Silvestrol (μM)
10-4 10-3 10-2 10-1 1
XBP1 mRNA
u
s
-300 bp
RocA (μM)
10-4 10-3 10-2 10-1 1
XBP1 mRNA
u
s
-300 bp
B
Tm VHC
ZTF VHC
Tm
ZTF
Mouse # 1 2 3 4 1 2 3 4 1 2 3 4 1 2 3 4
XBP1 mRNA
u*
s
-200 bp
GAPDH mRNA
-200 bp
XBP1 splicing (%) 3.3±1.4 3.1±1.4 37±10.3 10.3±4.1
C
CHX (μM)
- 10-2 10-1 1 10 102
XBP1 mRNA
u
s
-300 bp
GAPDH mRNA
-400 bp
EME (μM)
- 10-2 10-1 1 10 102
XBP1 mRNA
u
s
-300 bp
GAPDH mRNA
-400 bp
D
RocA (μM)
SEC61-IN-1 (μM)
CADA (μM)
DTT - 10-3 10-2 10-1 1
DTT - 10-2 10-1 1 10
- 10-3 10-2 10-1 1 10
GFP-ATF6-FL
GFP-ATF6-N
-150 kDa
-100 kDa
-75 kDa
VCL
-117 kDa
PERK-P
PERK
-125 kDa
VCL
-117 kDa
Lanes 1 2 3 4 5 6 7 8 9 10 11 12 13 14 15 16 17 18

Figure S6

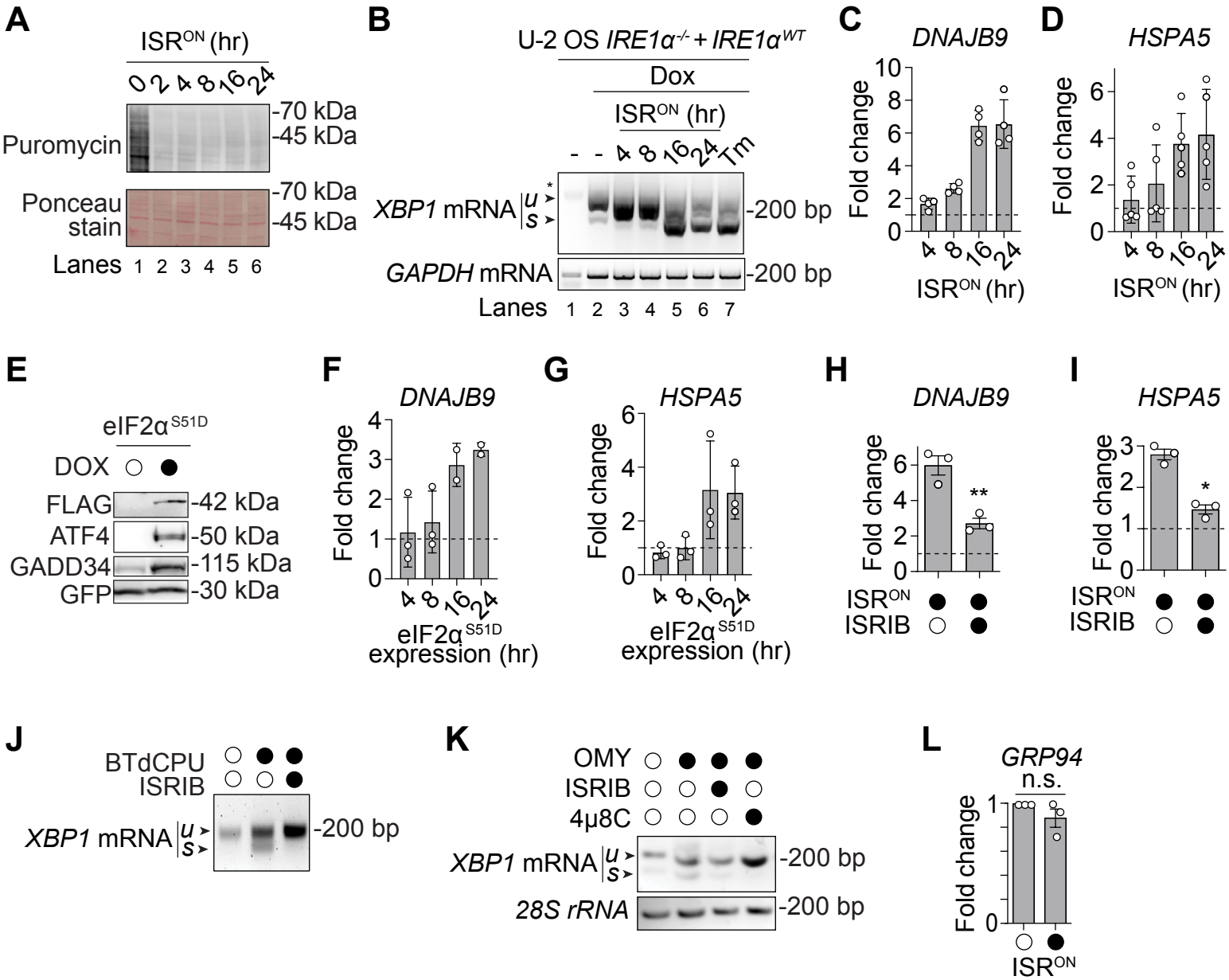
A
ISR^ON (hr)
0 2 4 8 16 24
Puromycin
-70 kDa
-45 kDa
Ponceau stain
-70 kDa
-45 kDa
Lanes 1 2 3 4 5 6
B
U-2 OS IRE1α-/- + IRE1α^WT
Dox
ISR^ON (hr)
- - 4 8 16 24 Tm
XBP1 mRNA
u
s
-200 bp
GAPDH mRNA
-200 bp
Lanes 1 2 3 4 5 6 7
C
DNAJB9
Fold change
ISR^ON (hr)
D
HSPA5
Fold change
ISR^ON (hr)
E
eIF2α^S51D
DOX
FLAG
-42 kDa
ATF4
-50 kDa
GADD34
-115 kDa
GFP
-30 kDa
F
DNAJB9
Fold change
eIF2α^S51D expression (hr)
G
HSPA5
Fold change
eIF2α^S51D expression (hr)
H
DNAJB9
Fold change
**
ISR^ON
ISRIB
I
HSPA5
Fold change
*
ISR^ON
ISRIB
J
BTdCPU
ISRIB
XBP1 mRNA
u
s
-200 bp
K
OMY
ISRIB
4μ8C
XBP1 mRNA
u
s
-200 bp
28S rRNA
-200 bp
L
GRP94
n.s.
Fold change
ISR^ON
M
IRE1α^WT-mNeonGreen
CTRL
ISR^ON
Tg
Inset
CTRL
ISR^ON
Tg

Figure S7

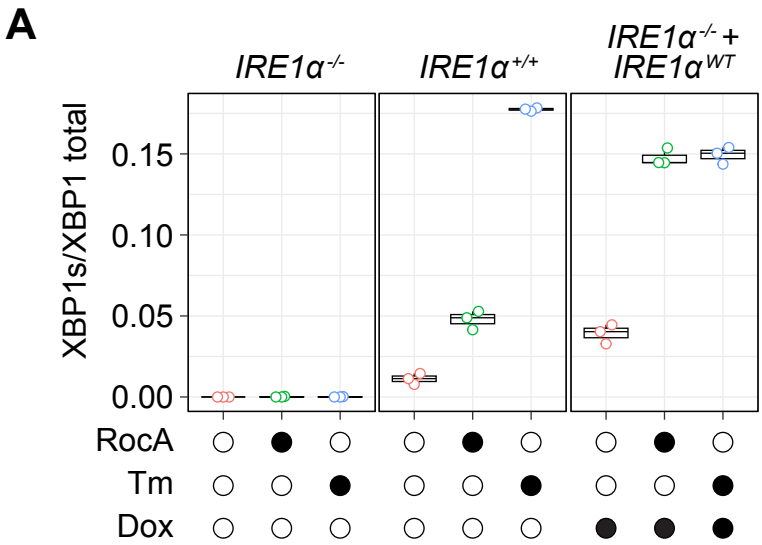
A
IRE1α-/-
IRE1α+/+
IRE1α-/- + IRE1αWT
XBP1s/XBP1 total
0.15
0.10
0.05
0.00
RocA
Tm
Dox

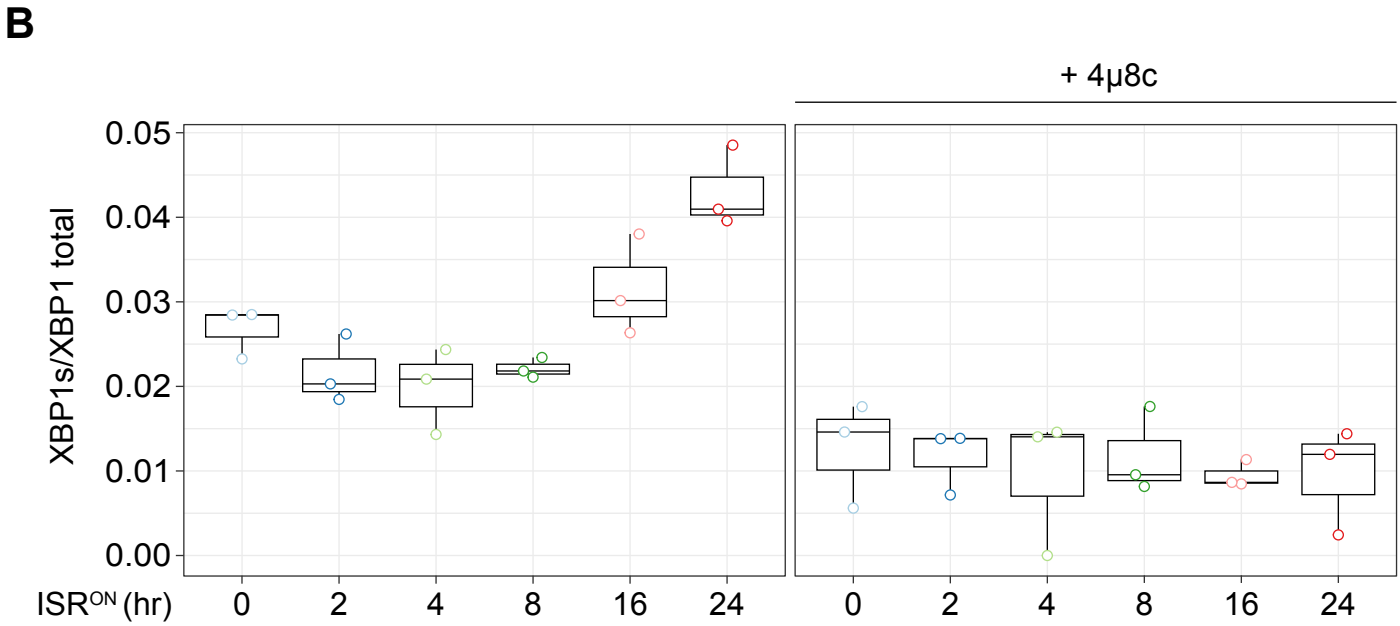
B
+ 4μ8c
XBP1s/XBP1 total
0.05
0.04
0.03
0.02
0.01
0.00
ISRON (hr)
0
2
4
8
16
24

Figure S8

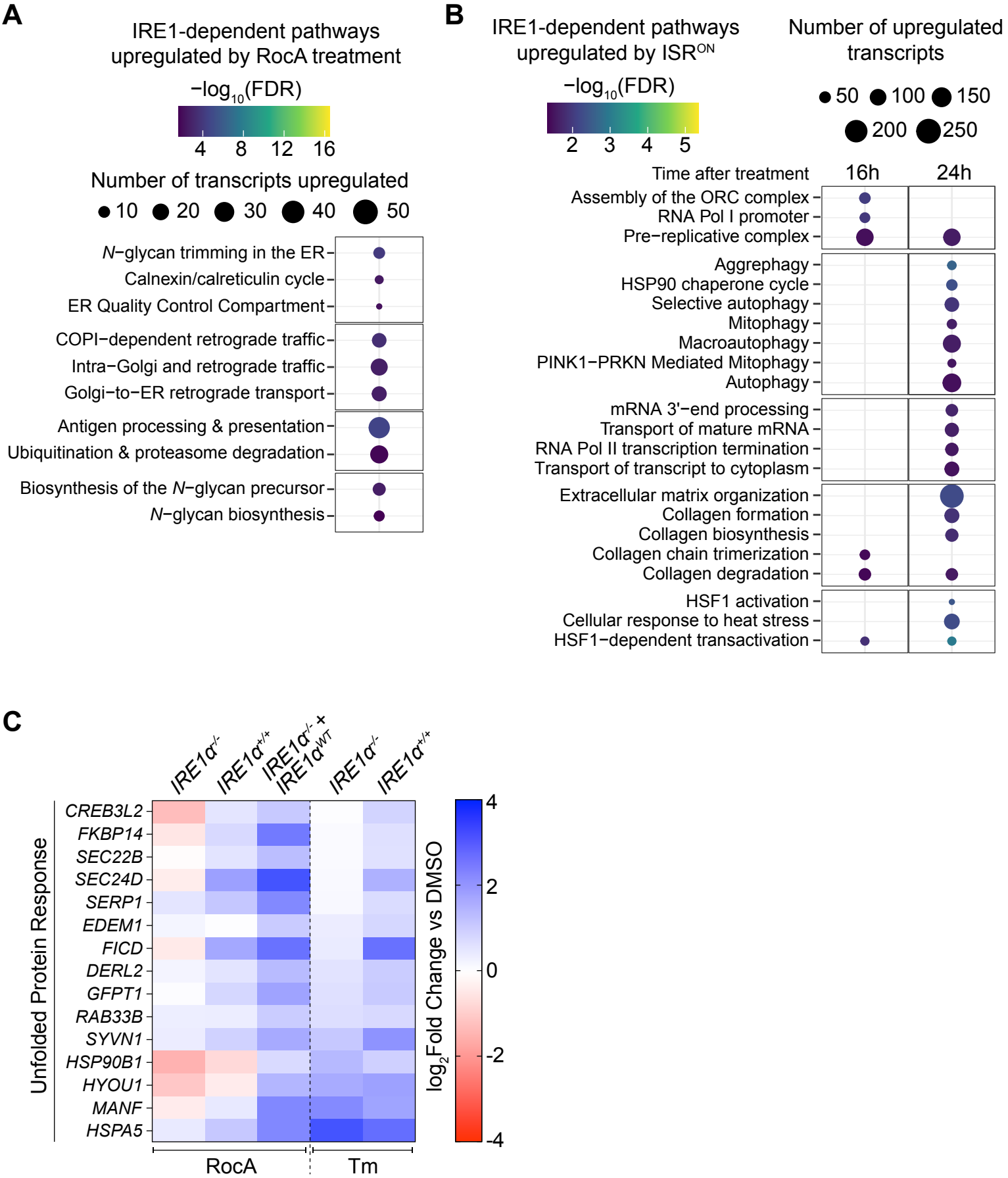
A
IRE1-dependent pathways upregulated by RocA treatment
−log10(FDR)
4 8 12 16
Number of transcripts upregulated
10 20 30 40 50
N−glycan trimming in the ER
Calnexin/calreticulin cycle
ER Quality Control Compartment
COPI−dependent retrograde traffic
Intra−Golgi and retrograde traffic
Golgi−to−ER retrograde transport
Antigen processing & presentation
Ubiquitination & proteasome degradation
Biosynthesis of the N−glycan precursor
N−glycan biosynthesis
B
IRE1-dependent pathways upregulated by ISRON
−log10(FDR)
2 3 4 5
Number of upregulated transcripts
50 100 150 200 250
Time after treatment
16h
24h
Assembly of the ORC complex
RNA Pol I promoter
Pre−replicative complex
Aggrephagy
HSP90 chaperone cycle
Selective autophagy
Mitophagy
Macroautophagy
PINK1−PRKN Mediated Mitophagy
Autophagy
mRNA 3'−end processing
Transport of mature mRNA
RNA Pol II transcription termination
Transport of transcript to cytoplasm
Extracellular matrix organization
Collagen formation
Collagen biosynthesis
Collagen chain trimerization
Collagen degradation
HSF1 activation
Cellular response to heat stress
HSF1−dependent transactivation
C
IRE1α−/−
IRE1α+/+
IRE1α−/− + IRE1αWT
IRE1α−/−
IRE1α+/+
Unfolded Protein Response
CREB3L2
FKBP14
SEC22B
SEC24D
SERP1
EDEM1
FICD
DERL2
GFPT1
RAB33B
SYVN1
HSP90B1
HYOU1
MANF
HSPA5
RocA
Tm
log2Fold Change vs DMSO
4
2
0
-2
-4